Mantle Origin and Flow Sorting of Megacryst-Xenolith Inclusions in Mafic Dikes of Black Canyon, Arizona

U.S. GEOLOGICAL SURVEY PROFESSIONAL PAPER 1541

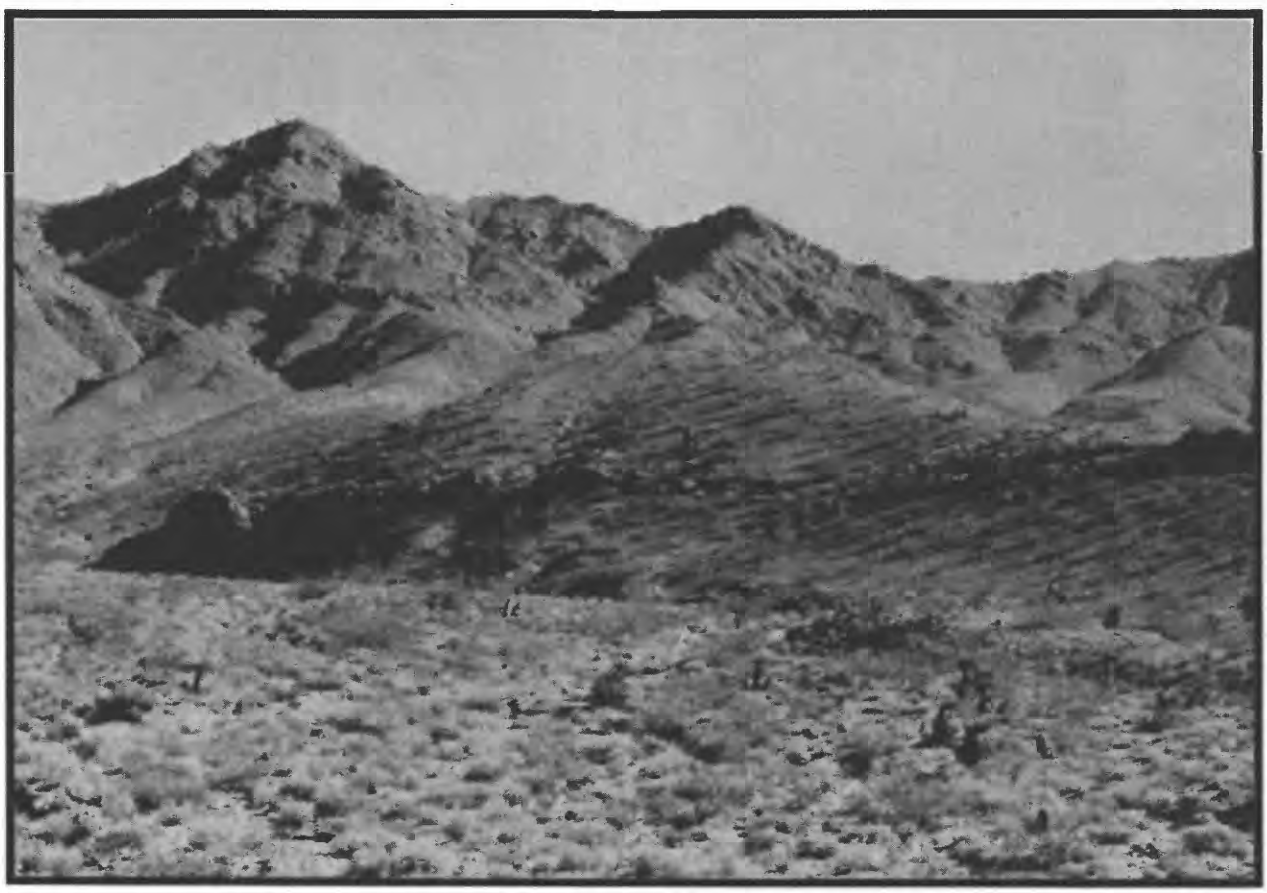

AVAILABILITY OF BOOKS AND MAPS OF THE U.S. GEOLOGICAL SURVEY

Instructions on ordering publications of the U.S. Geological Survey, along with prices of the last offerings, are given in the current-year issues of the monthly catalog "New Publications of the U.S. Geological Survey." Prices of available U.S. Geological Survey publications released prior to the current year are listed in the most recent annual "Price and Availability List." Publications that are listed in various U.S. Geological Survey catalogs (**see back inside cover**) but not listed in the most recent annual "Price and Availability List" are no longer available.

Reports released through the NTIS may be obtained by writing to the National Technical Information Service, U.S. Department of Commerce, Springfield, VA 22161; please include NTIS report number with inquiry.

Order U.S. Geological Survey publications **by mail** or **over the counter** from the offices given below.

BY MAIL

Books

Professional Papers, Bulletins, Water-Supply Papers, Techniques of Water-Resources Investigations, Circulars, publications of general interest (such as leaflets, pamphlets, booklets), single copies of Earthquakes & Volcanoes, Preliminary Determination of Epicenters, and some miscellaneous reports, including some of the foregoing series that have gone out of print at the Superintendent of Documents, are obtainable by mail from

U.S. Geological Survey, Map Distribution
Box 25286, MS 306, Federal Center
Denver, CO 80225

Subscriptions to periodicals (Earthquakes & Volcanoes and Preliminary Determination of Epicenters) can be obtained ONLY from the

Superintendent of Documents
Government Printing Office
Washington, DC 20402

(Check or money order must be payable to Superintendent of Documents.)

Maps

For maps, address mail orders to

U.S. Geological Survey, Map Distribution
Box 25286, Bldg. 810, Federal Center
Denver, CO 80225

Residents of Alaska may order maps from

U.S. Geological Survey, Earth Science Information Center
101 Twelfth Ave., Box 12
Fairbanks, AK 99701

OVER THE COUNTER

Books and Maps

Books and maps of the U.S. Geological Survey are available over the counter at the following U.S. Geological Survey offices, all of which are authorized agents of the Superintendent of Documents.

- **ANCHORAGE, Alaska**—4230 University Dr., Rm. 101
- **LAKEWOOD, Colorado**—Federal Center, Bldg. 810
- **MENLO PARK, California**—Bldg. 3, Rm. 3128, 345 Middlefield Rd.
- **RESTON, Virginia**—National Center, Rm. 1C402, 12201 Sunrise Valley Dr.
- **SALT LAKE CITY, Utah**—Federal Bldg., Rm. 8105, 125 South State St.
- **SPOKANE, Washington**—U.S. Post Office Bldg., Rm. 135, W. 904 Riverside Ave.
- **WASHINGTON, D.C.**—Main Interior Bldg., Rm. 2650, 18th and C Sts., NW.

Maps Only

Maps may be purchased over the counter at the U.S. Geological Survey offices:

- **FAIRBANKS, Alaska**—New Federal Building, 101 Twelfth Ave.
- **ROLLA, Missouri**—1400 Independence Rd.
- **STENNIS SPACE CENTER, Mississippi**—Bldg. 3101

Mantle Origin and Flow Sorting of Megacryst-Xenolith Inclusions in Mafic Dikes of Black Canyon, Arizona

By Jane E. Nielson *and* John K. Nakata

U.S. GEOLOGICAL SURVEY PROFESSIONAL PAPER 1541

UNITED STATES GOVERNMENT PRINTING OFFICE, WASHINGTON : 1994

U.S. DEPARTMENT OF THE INTERIOR
BRUCE BABBITT, Secretary

U.S. GEOLOGICAL SURVEY
Robert M. Hirsch, Acting Director

For sale by
U.S. Geological Survey, Map Distribution
Box 25286, MS 306, Federal Center
Denver, CO 80225

Text and illustrations edited by James W. Hendley II

Library of Congress Cataloging-in-Publication Data

Nielson, Jane E.
Mantle origin and flow sorting of megacryst-xenolith inclusions in mafic dikes of Black Canyon, Arizona / by Jane E. Nielson and John K. Nakata.
p. cm.—(U.S. Geological Survey professional paper ; 1541)
Includes bibliographical references.
Supt. of Docs. no.: I9.16:1541
1. Basalt—Inclusions—Black Canyon (Ariz. and Nev.) 2. Geology, Stratigraphic—Miocene. 3. Geology, Stratigraphic—Pliocene. 4. Geology—Arizona. I. Nakata, John K. II. Title. III. Series.
QE462.B3N54 1994
552'.26'0979159—dc20 93-23011
CIP

Cover—Segment of north-trending dike array in Black Canyon, Arizona. Tabular dike segment crosses fanglomerate ridge. At north end (left), dike incorporated a mass of the host fanglomerate and developed a bulbous swelling. Wilson Ridge in background.

CONTENTS

FIGURES

TABLES

Mantle Origin and Flow Sorting of Megacryst-Xenolith Inclusions in Mafic Dikes of Black Canyon, Arizona

By Jane E. Nielson *and* John K. Nakata

ABSTRACT

Three arrays of inclusion-bearing alkali basalt dikes, 1 to 1.5 km in length, crop out in Miocene and Pliocene fanglomerate in Black Canyon, near the Colorado River, northwest Arizona. Erroneously called camptonite dikes, the best known exposures are in a series of roadcuts about 16 km south of Hoover Dam. The origin of axial concentrations of inclusions in these dikes has long been debated. The north-trending dike arrays consist of at least 16 short segments, which are 61 to 366 m in length. Five of these segments pinch out at the north or south end, or both; where the tips of dike segments overlap, they may be deflected in opposite directions. These stress-related deflections show that the segments of each array were emplaced concurrently.

A vent area of related tuff breccia and multiple intrusions crops out at the south end of the dike arrays. The dikes, related tuff breccia, and a possible small lava flow all contain inclusions. Although the most distinctive inclusions are mafic to ultramafic mineral fragments (megacrysts) and xenoliths, the largest and most common inclusions are silicic igneous and metamorphic rocks from disaggregated masses of fanglomerate wall rock. Compositions of the suite of mafic megacrysts indicate derivation from the mantle; thus they are xenocrysts. The alkali olivine basalt composition inferred for the juvenile magma of Black Canyon dikes and eruptive units is consistent with these inclusion compositions.

The dominant mantle-derived megacrysts are black kaersutite (Ti-hornblende) cleavage fragments with ubiquitous reaction textures. Less common xenocrysts are black pyroxene grains and polygranular olivine clusters. Small xenoliths of spinel peridotite and pyroxenite—including amphibole- and mica-bearing types—are present but uncommon; one peridotite contains a kaersutite veinlet with compositions similar to most analyzed kaersutite megacrysts. Systematic analyses of kaersutite grains from the dike segment with the best-exposed inclusion concentration show no compositional variations that can be related to grain size, shape, textural relations, or position. Mineral compositions and textural relations indicate that the mafic xenolith-megacryst (xenocryst) assemblage in the Black Canyon dikes most likely was derived from an area of upper mantle composed of peridotite with veins of pyroxenite and pods of coarse crystalline amphibole. Partial melting of this type of assemblage could have produced the dike magma, but the observed reaction textures and isotopic disequilibrium between megacrysts and the dike matrix indicate that the suite of inclusions does not represent the actual parent material.

Our detailed observations indicate that most internal structures in the dikes are concordant with the axial planes of the dike segments and are related to flow processes of magma in conduits. These structures include: alternating zones of massive or fissile matrix (containing longitudinal joints), rare flow banding, and the boundaries of matrix structure zones, as well as orientations of the long dimensions of vesicles and of mineral and rock inclusions. One roadcut through a dike segment exhibits four to five regularly-alternating matrix structure zones in combination with a large volume of size-sorted inclusions.

Only three dike segments contain more than 10 percent inclusions. In all these segments the largest volume of inclusions—of both mantle and near-surface origin—is concentrated in the axial zones; the largest inclusions and the greatest size range of inclusions are found in the central zone of the dike. The presence of fanglomerate clasts in these axial inclusion concentrations demonstrates that inter-grain pressures effectively moved inclusions toward the center of the dike conduits. Therefore, axial concentrations of mantle xenolith-xenocryst inclusions are found in the dikes where the flowing magma contained a relatively large volume of particles. The axial inclusion concentrations and size sorting of inclusions were most likely produced by flow sorting and not by multiple injections of magma or progressive crystallization phenomena, which have been proposed previously.

Manuscript approved for publication May 12, 1993

INTRODUCTION

Alkali olivine basalt dikes and dike-fed tuff breccia crop out in an area of approximately 1.5 km^2, near U.S.

Highway 93, in the Black Canyon of the Colorado River, northwest Arizona. The best-known dike exposure is a roadcut located 16 km south of Hoover Dam and the tuff breccia is found in a small eruptive center, located at the south end of dike outcrops (figs. 1 and 2). The dikes were

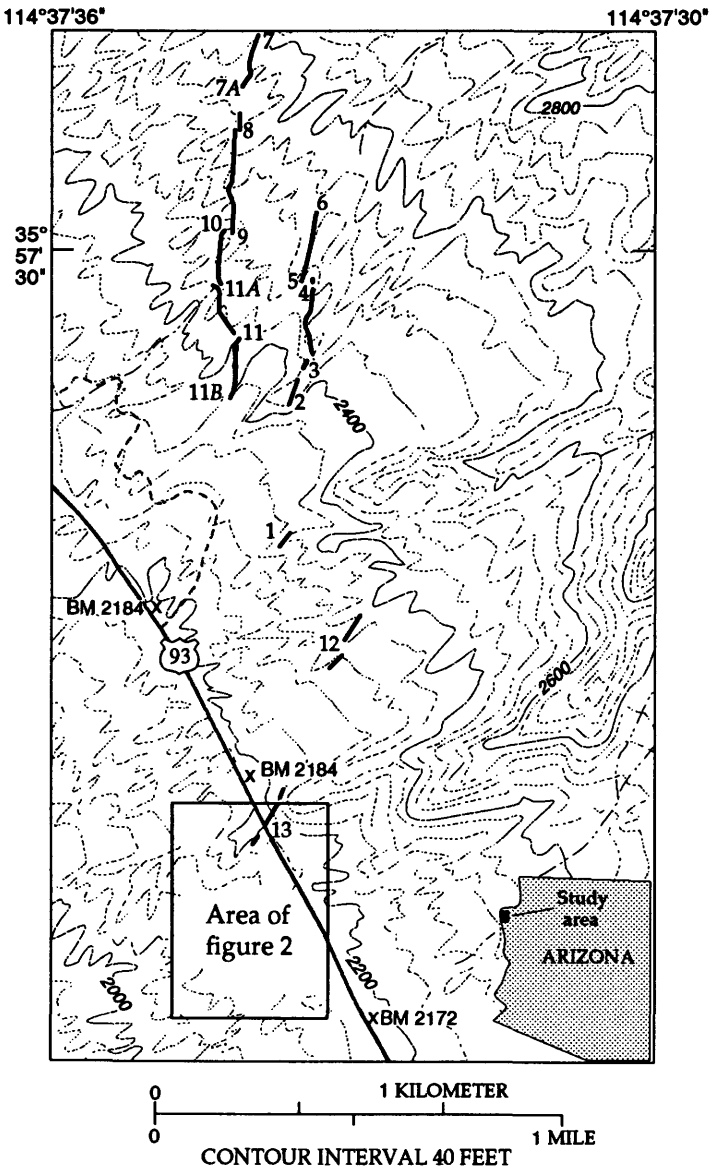

Figure 1. Index map of study area, in northwestern Arizona. Dikes are shown in heavy black lines; numbered locations are described in table 1 and text. Heavy dashed line represents a jeep trail. Topographic base from U.S. Geological Survey Ringbolt Rapids, Arizona-Nevada quadrangle map, 1:24,000 scale, photorevised 1973.

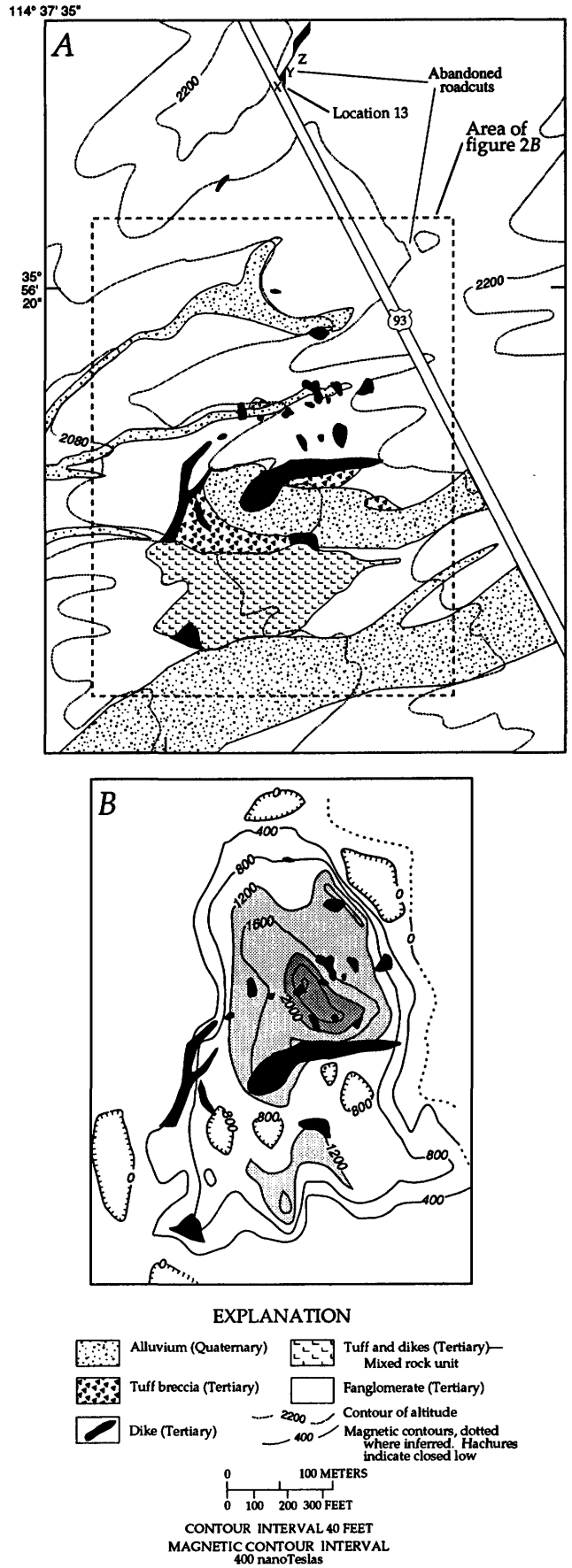

Figure 2. *A*, Map showing geology of vent area and southernmost dikes of southern Black Canyon array (location shown in fig. 1). *B*, Map showing the magnetic expression of the vent area, superimposed on outcrops of intrusions (location shown in fig. 2*A*). Light shading shows main region of domed magnetic anomaly; darker shading is the highest peak on the magnetic anomaly.

emplaced in fanglomerate of Miocene and Pliocene age, which contains clasts derived from older metamorphic rocks and granite of the adjacent mountain ranges.

Roadcuts expose a dike segment with conspicuous concentrations of kaersutite megacrysts and rock fragments; inward from the contacts the kaersutite grains increase in abundance and are larger in size. These concentrations were called "zoning" by Campbell and Schenk (1950), who interpreted the dike as a camptonite magma that had crystallized in place. They hypothesized that volatile components of the magma had been concentrated in the axial zone of the dike, allowing crystallization of coarse kaersutite grains, and that smaller crystals formed in the dike margin, owing to the smaller proportion of volatiles in the magma near dike contacts. However, rock fragments also are larger in the dike axial zone, and xenoliths of altered peridotite, probably of mantle origin, have been identified in the inclusion suite (Wilshire, Schwarzman, and Trask, 1971). Compositions of kaersutite and pyroxene megacrysts from the roadcut exposures suggested that these minerals also were derived from a mantle source (Best, 1974; Irving, 1977; Basu, 1978; Boettcher and O'Neil, 1980; Foland and others, 1980; Garcia and others, 1980).

Our detailed study of structures, textures, and inclusion content and distributions in all the exposed dike segments verifies the mantle origin of the mafic megacrysts and xenoliths. Thus, the kaersutites did not crystallize in place. Moreover, the distribution of inclusions by size are more complex than Campbell and Schenk (1950) indicated, and we conclude that neither inclusion concentrations nor the size distribution in various dike segments could have originated as those authors proposed. We also found that longitudinal zones, defined by alternations of massive matrix and dike-parallel fissile joints, are ubiquitous and that only two other exposed dike segments of the Black Canyon arrays contain inclusion concentrations similar to those in the well-known highway roadcuts. Therefore, the "zoning" observed in the highway roadcut is a coincidence of features that occur in various combinations throughout the exposures of dikes in Black Canyon.

ACKNOWLEDGMENTS

We especially thank Howard Wilshire who originally suggested that "zoning" in the Black Canyon dikes was due to flow sorting, and Myron Best whose early encouragement kept us going. W.A. Duffield and E.I. Smith provided careful and constructive reviews that led to substantial improvements in the manuscript. Determinations of oxygen and carbon isotopic compositions were done by L.D. White, through the courtesy of Ivan Barnes and J.R. O'Neil. Whole-rock major-element compositions were analyzed by J. Baker, A.J. Bartel, K.C. Stewart, J.E. Taggart, and J.S. Wahlberg. Volatile elements were determined by P.R. Klock, G. Mason, H.M. Neiman, S. MacPherson, and C. Stone. Dennis Sorg prepared the leached rock powders for analysis. Between 1981 and 1985, field support was provided by Jay Noller, Tova Diamond, and Cynthia Ardito.

Modeling of natural remanent magnetization (NRM) was suggested by Bob Simpson, who provided the magnetic susceptibility bridge for those measurements; Ray Wells guided us in collection of oriented samples for NRM determinations, and those measurements were performed by Vicki Pease. Andrew Griscom provided a magnetometer for traverses of the vent area. Todd Fitzgibbon, Linnea Larsen, and Ruby Harper helped with data and word processing. Various parts of the study were prompted by observations of features in the Black Canyon dikes, communicated orally or in reviews by Steve Bergman, Ray Binns, Dave Eggler, Mike Garcia, and Frank Spera.

GEOLOGIC RELATIONS IN BLACK CANYON

The Black Canyon dikes comprise three distinct arrays of discontinuously exposed dike segments. Two subparallel arrays, 1 and 1.5 km long, trend close to due north (fig. 1). Exposed dike segments in each array are from 61 to 366 m long (table 1). A third, more dispersed array with a northeasterly trend is 1 km long and comprises dike segments 60 to 160 m long (fig. 1). This third set of dikes trends into related eruptive deposits and intrusions at the south end of the study area (fig. 2).

The Black Canyon dikes intrude gently west-dipping Miocene and Pliocene fanglomerate deposits of the Muddy Creek Formation. The fanglomerate forms an alluvial apron along the west flank of north-trending mountain ranges, from which clasts of Precambrian gneiss and granite were derived. Volcanic rocks of early to middle Miocene age underlie fanglomerate west of the dike arrays; these rocks are mostly andesite and dacite with subordinate basalt and include dacite airfall and ash-flow tuff (Anderson and others, 1972; Anderson, 1978; E.I. Smith, written commun., 1988). Mesa-capping flows of aphyric basalt locally overlie the fanglomerate and Precambrian rocks (Anderson and others, 1972).

The dikes have K-Ar ages of 4 to 5 Ma (Anderson and others, 1972), and ages of 3.7 to 5.8 Ma are reported for massive mesa-capping basalts (Anderson and others, 1972). The megacryst-bearing dikes are distinctly different in composition and appearance from the bulk of approximately coeval basalt flows (Campbell and Schenk, 1950). Thus, the megacryst-bearing dikes probably were not feeders for these mesa-capping flows.

Table 1. Characteristics of Black Canyon dikes.

Dike segment (see fig. 1)	Description	Attitude		Width (cm)[1]		Length (m)	Comments
		Strike	Dip	Min.	Max.		
1	Short segment, outcrops 900 m north of highway.	N20°E	79°W	80	150	61	Tabular, with horizontal cooling joints. Matrix fissile in axis. Sparse inclusions, kaersutite, olivine predominate.
2	Crops out on fanglomerate ridge, east of jeep trail; 2 segments with about 70-m gap between exposures.	N16°E	90°	91	370	213	South end tabular, no zoning. Bulbous swelling at north end, adjacent to tabular segment with 5 massive to fissile zones. Abundant inclusions; fanglomerate clasts predominate, kaersutite less abundant.
3 to 4	Sinuous, offset from north end of segment 2. Segment 3 is south end, 4 north end, of dike.	N02°W to N35°E	90°	0	1,110	275	Predominantly tabular, 3 interior zones. Mass of fanglomerate inclusions at contact near south end. Sparse inclusions, all in axis near north end; kaersutite predominates. No size sorting. Bulbous swelling at north end near dike tip.
5 to 6	Northernmost exposure of eastern array. West contact is not exposed.	N10°E	71°E	0	115	275	Bulbous swelling predominant in outcrop. Two asymmetric zones, sparse inclusions; predominantly kaersutite. No size sorting.
7	Northernmost exposure of western array.	N02°E to N15°E	90°	0	100	183	Tabular, resembles segment 1. Tip exposed at north end, near small dam in wash.
7*A* to 8	Relatively straight segment, some unexposed parts.	N10°E	90°	0	180	152	Tabular, massive contact, fissile axis zones. Sparse inclusions; kaersutite predominant. No size sorting. Tip exposed at south end.
8 to 9	Relatively long and straight segment.	N20°E	90°	110	280	366	Tabular, resembles segments 7*A* to 8. Forms large and small dams across 2 washes.
10 to 11*A*	Straight segment, but tip at south end deflected sharply to northwest.	N	90°	0	100	150	Tabular, massive contact, fissile inner zone, and massive axial zone. No size sorting.
11*A* to 11	Sinuous segment. Parabolic tips at both ends.	N10°E to N11°W	76°W	0	240	244	Tabular, 2 asymmetric zones. Small bulbous swelling near north end. Sparse inclusions, no size sorting. Forms large dam in wash.
11 to 11*B*	Sinuous segment. At north end is well exposed parabolic tip.	N05°E to N10°W	90°	0	255	245	Tabular, no distinct zones or size sorting; sparse kaersutite inclusions. Parabolic joints concentric to contact in tip exposed at north end.
12	Two short segments in large wash between highway and Station 1.	N25°E	90°	60	100	200	Tabular and massive. No zones; sparse inclusions, predominantly kaersutite.
13	Cross section exposed in U.S. Highway 93 roadcuts.	N25°E	78°E	115	160	244	Tabular, 5 alternating zones, massive to fissile zones. Inclusion concentrations, marked size sorting. Highest inclusion abundances observed; kaersutite predominant.

[1]All widths measured perpendicular to the local axial plane of the dike.

EXTRUSIVE AND INTRUSIVE MEGACRYST-BEARING ROCKS

VENT AREA

The vent area exposes pyroclastic tuff breccia and irregularly-shaped intrusions (fig. 2*A*). The apparent subsurface extent of intrusions is defined by a magnetic survey, described below. Although the area appears very complex, the essential relations can be simply summarized: (1) No exposures show interstratification of pyroclastic rocks and fanglomerate; and (2) outcrop relations and magnetic anomalies indicate that the contact between the fanglomerate and the complex of related volcanic and intrusive rocks is steep near the southernmost boundary. This contact defines the margin of the eruptive vent.

Dikes intrude both tuff breccia and fanglomerate in the northern part of the vent area. In the southern part of the vent area a unit of mixed rocks most likely consists of tuff breccia and intrusions, although a part of the exposure may be an eroded lava flow remnant (fig. 2*A*). Irregular blocks of jointed aphyric basalt are found locally, and these may be accidental inclusions derived from older Miocene lava. However, the most massive dike in the vent area, which intrudes the contact between tuff breccia and fanglomerate, grades from holocrystalline and inclusion bearing to massive and aphyric. Most other outcrops of aphyric basalt are poorly exposed, and their relation to intrusions of the vent area remains unclear.

TUFF BRECCIA DEPOSITS

The pyroclastic deposits are buff-colored or red to red-brown, massive to bedded mafic tuff breccia; layering is crude and localized in the southwestern part of the vent area (fig. 2*A*). Matrix of the bedded tuff breccia is mostly clay and arkosic sand that probably derives from fanglomerate. The matrix also includes small grains of kaersutite, olivine, and vesicular lava. Clasts include gneiss and granite from the fanglomerate, kaersutite megacrysts as much as 1.5 cm across, and irregular masses of vesicular lava as much as 20 cm across. Some beds contain flattened masses of clay, which may be accretionary lapilli. In the southern part of the vent area, tuff breccia layers and interleaved sills dip 25° to the east. The continuity of dips in all other units suggests that the bedded tuff probably was tilted by the upwelling intrusive magma. The bedded tuff breccia locally is friable, but near intrusive contacts it is metamorphosed to a tough, flinty rock.

Massive light-colored tuff breccia that resembles vent agglomerate forms a small outcrop in the northern part of the vent area. It is composed of angular scoria fragments and has a lower content of mafic megacrysts, clay, and sand than the bedded tuff breccia. Contact relations between the massive and bedded breccia deposits are unexposed.

INTRUSIONS

Mafic intrusions that contain kaersutite megacrysts occur throughout the vent area. In the south part of the vent area, several dikes intrude the contact between ejecta and fanglomerate on the west side (fig. 2*A*); oval pieces of massive aphyric basalt 0.5 to 1 m across are found in these intrusions. The matrix of the fanglomerate is reddened at distances as much as 70 cm from the contacts with these dikes. The most prominent of the dikes strikes N. 25° E. to N. 10° E. and has dips that vary from moderate to steep (as much as 78° southeast). This tabular dike contains columnar cooling joints that are perpendicular to the dike walls; because of the vertical to subhorizontal change in the dike orientation, the columnar joints also vary from subhorizontal to subvertical.

A few meters north of the northernmost outcrop of tuff breccia, several dikes intrude fanglomerate; a cross section of the largest of these dikes is exposed in a wash. The chilled contact between the dike and the fanglomerate is irregular, and the dike itself has a bulbous shape that is roughly oval in cross section (fig. 3). The internal structure is complex, with zones of chilled magma next to masses of partly disaggregated fanglomerate. Gradational between the areas of chilled magma and fanglomerate is pépérite-like breccia of magma and sandy matrix from the fanglomerate.

Figure 3. Bulbous intrusion in fanglomerate at north end of both vent area and outcrop; scale given by seated figure in light hat (at base). Along the top of the fanglomerate ridge, the dike appears tabular.

MAGNETIC EXPRESSION OF THE VENT AREA

A ground-level magnetic survey was made of the vent area to determine the extent and probable shape of the intrusions. Traverses to measure the vertical component of the magnetic field were made with a fluxgate magnetometer, from a baseline oriented N. 70° W., located 50 m south of the southernmost dike exposure. Approximately north-south lines of traverse were established at 32-m spacings along the baseline. Measurements were made at 50-ft (16 m) intervals, resulting in a rectangular grid of data points over an area 500×400 m. The magnetic background was determined to be 250 gammas, from the average readings made over fanglomerate along the baseline; values are believed accurate to ±10 gammas (1 gamma=1 nanoTesla). Data were corrected for diurnal drift by readings taken at baseline station 1 at the beginning and end of each traverse.

Magnetic susceptibilities of the dikes were measured in the field using a hand-held susceptibility meter. Selected samples also were measured in the laboratory with a susceptibility bridge. The natural remanent magnetization (NRM) of the samples was measured in the laboratory on oriented hand samples. The NRM direction has normal polarity, and for five of the nine samples it points in the direction of the present-day field. Magnetic susceptibilities (measured in the cgs system) for all samples range from 2.6×10^{-3} to 17×10^{-3}. Seven of the nine samples have susceptibilities from 2.6×10^{-3} to 4.76×10^{-3}, with a median value of 3.5×10^{-3}.

A domed magnetic anomaly (average readings between 650 and 1,050 gammas; fig. 2*B*), with steep marginal gradients, was recorded in the northern part of the vent area; sharp anomalies peak at 2800 gammas (light and heavy shaded areas, fig. 2*B*). The shape of this anomaly indicates that exposures are connected to an intrusive body or multiple intrusive bodies beneath the vent area; the steep marginal gradients indicate that the intrusive mass is relatively shallow. Another area of high anomalous values (1,200 to 1,600 gammas) was detected in the southern and southwestern part of the vent area (light shaded area, fig. 2*B*). This southern anomaly is coincident with the outcrops of mixed tuff breccia and intrusions (mixed rocks unit, fig. 2*A*).

The essential features of the measured magnetic field in the vent area are represented well by a two-dimensional model of a uniformly magnetized body at shallow depth. To model the amplitude of the observed anomaly, magnetization values of 5×10^{-3} were required; these are the highest measurements on seven of nine surface exposures. The sharp peaks and valleys of the anomaly can be explained by assuming irregularities in the upper boundary of the body. We also considered an alternative model of a body that consists of a variably magnetized intrusion or complex of intrusions, which could explain the essential features of the anomaly equally as well.

Bodies 50 and 200 m in thickness were tested in the model of a uniformly magnetized body; solutions for each body thickness match the essential features of the anomaly. Thus, the data provide few constraints on depth or shape of the base of the magnetic intrusive mass.

On the south and west margins of the vent area, the 400-gamma magnetic contour bounds the two-dimensional model body. Steep magnetic gradients at these margins are explained well by assuming nearly vertical contacts, which may correspond either to faults or steep intrusive contacts. However, the east and north boundaries of the vent area are modeled best by contacts with relatively shallow outward dips. For a model body with steep contacts, a well-defined magnetic polarization low is expected north of the vent area. The absence of this polarization low supports the idea that the magnetic body has a northern contact with a shallow north dip.

This simple model of a single, uniformly magnetized body explains the anomaly. However, we prefer the alternative model of many variably magnetized intrusions because it is consistent with field observations, which indicate that the magnetic body is a composite of intrusions. Because the NRM of dikes in the vent area and the present-day field have the same direction of magnetization, the high average magnetization used to model the amplitude of the observed anomaly can be justified as an effect of additive magnetizations from several individual intrusions.

OBSERVATIONS ON THE DIKE ARRAYS

GEOLOGIC RELATIONS AND STRUCTURES

Three discontinuous arrays of offset dike segments crop out north and northeast of the vent area in Black Canyon (fig. 1). The southernmost array has predominantly N. 25° E. strikes, and the two northernmost arrays have predominantly N. 0° E. to N. 10° E. trends and steep dips (75° to 85°) to the east (table 1). Some of the north-trending dike segments are sinuous, with local strikes up to N. 10° W. (fig. 1). Only one dike segment (between locations 11 and 11*A*, fig. 1) strikes northwest along the entire length of exposure. All other Miocene dikes in the study area, including mafic and silicic varieties, have northerly orientations (Anderson, 1978).

The contacts between dikes and fanglomerate are sharp, and all dikes have distinct chilled margins (table 2). The fanglomerate shows slight but distinct reddening as much as 300 cm from the contacts, owing to the thermal effects of dike emplacement. Clasts and sandy matrix that clearly came from incorporation of fanglomerate wall rocks are found locally in the dikes.

No faults are apparent in the fanglomerate deposits; however, numerous north-trending high-angle normal faults occur in older Miocene rocks, which are exposed 5 to 10 km

Table 2. Features of zoned dikes.

[—, no data; n.d., data not determined]

Dike segment (see fig. 1)	Zone	Width (cm)	Inclusion abundance[1]	Inclusion size (mm)		Matrix texture	Matrix structure	Comments
				Max.	Min.			
2	1	1–2	Sparse to barren	—	—	Glassy	Massive	Symmetrical chilled margin.
	2	2–5	Sparse	—	—	Glassy to very fine grained	Massive	Inner chill zone.
	3	15–25	Abundant	0.5–30	n.d.	Fine grained	Sparsely fissile	Zones symmetrical to axis; "braided" matrix structure. Kaersutite, olivine inclusions predominate.
	4	110–130	Very abundant	5–70	?–50	Indeterminate	Massive	Axis contains granite, gneiss clasts to 70 mm. Less abundant kaersutite to 50 mm.
3	1	10–20	Abundant	0.1–25	n.d.	Glassy, vesicular	Massive	Chilled contact.
	2	70	Sparse	0.8–20	n.d.–2	Very fine grained	Sparsely fissile	Symmetrical to axis.
	3	140	Abundant	0.1–70	n.d.	Very fine grained to fine grained	Variably fissile	Axial zone varies irregularly from massive to fissile.
4	1	10–25	Sparse	0.5–20	n.d.	Glassy to very fine grained	Massive	Chilled contact. Rare flow banding parallel to contact.
	2	56–145	Sparse	0.5–25	n.d.	Fine grained	Variably fissile	Symmetrical to axis, varies in width.
	3	25–50	Sparse to moderately abundant	0.3–25	n.d.	Fine grained	Fissile	Inclusions concentrated in axial zone.
5 to 6	1	?–20	Sparse	0.2–20	n.d.	—	Massive	West half of dike; contact not exposed.
	2	95	Sparse	1.0–50	n.d.	—	Fissile	East half of dike.
10 to 11	1	20–43	Sparse	?–20	n.d.	—	Massive	Contact and chilled margin.
	2	24–41	Barren	n.d.	n.d.	—	Fissile	
	3	87–100	Sparse	1.5–60	n.d.	—	Massive	Zone absent north of location 11*A*.
13X,Y, Z	1	3–13	2	0.5–5	0.1–2	Glassy, vesicular	Massive	Symmetrical contact, in all exposures.
	2	7–18	5–6	0.5–20	0.1–4	Very fine grained, vesicular	Sparsely fissile	Symmetrical in all exposures. Contact of zones 1–2 gradational.
	3	18–40	25–30	0.5–40	0.1–6	Fine grained, vesicular	Highly fissile	Symmetrical to axis in Y, Z; occurs W side of axial zone of exposure X.
	4	20–40	13–15	0.5–40	0.1–6	Fine grained, amygdaloidal	Massive	Symmetrical in exposure Z; absent in Y; occurs only E side of axis in exposure X.
	5	15–40	13–40	0.5–72	2–12	Fine grained, amygdaloidal	Highly fissile	Axial zone always present; gradational to zones 3 and (or) 4.

[1]Qualitative estimates, except for location 13, for which numbers are mode percents (field mode); see figure 13*C*.

west of U.S. Highway 93 (Anderson, 1978). The Black Canyon dike and fault trends also are parallel to those of nearby mountain ranges and thus probably are parallel to unexposed range-front faults. Miocene extension in an east-west direction is well documented to the west of Black Canyon in the nearby Eldorado Mountains of Nevada and to the south of Black Canyon in the Colorado River trough (Anderson, 1971, 1978; Anderson and others, 1972; Howard and John, 1987; Faulds and others, 1990). Thus, Black Canyon dike arrays are oriented nearly perpendicular to the direction of Miocene extension and parallel to the direction of least horizontal stress at the time of dike emplacement.

Most dike segments crop out continuously (fig. 1) and are best exposed on the lower slopes of dissected alluvial fans, although some outcrops can be followed across interfluves. Gaps along strike occur on ridges where dike crests have not been exposed by erosion. Most of the large open areas between dike segments are washes with alluvial fill and may be due either to the level of exposure or the absence of an intrusion in those areas. Dikes that cross narrow washes commonly form sediment dams (table 1; Campbell and Schenk, 1950).

With notable exceptions, dikes typically are tabular and range in width ("thickness" as defined by Delaney and Pollard, 1981) from 80 to 370 cm (table 1). Widths decrease abruptly near the parabolic tips where dike segments pinch out. Few tips are seen in outcrop; the best exposed tip is at location 11*B* (table 1; figs. 1 and 4). At locations 2, 4, between 5 and 6, and at 11 the otherwise tabular dike segments display bulbous swellings ("protrusions" of Campbell and Schenk, 1950; "buds" of Delaney and Pollard, 1981) that are up to 1,110 cm wide (table 1; figs. 5 and 6*A*, *B*). Bulbous swellings occur both in the middle and near ends of tabular segments.

Magnetic anomalies of the thin vertical Black Canyon dikes are observed only when the magnetometer is directly

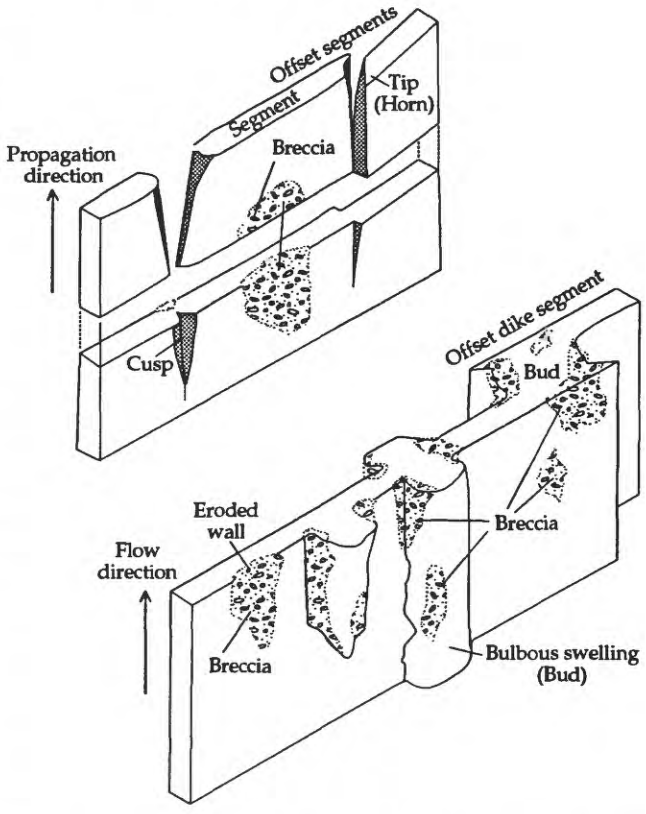

Figure 5. Idealized dike (from Delaney and Pollard, 1981) based on study of northeastern dike at Shiprock, New Mexico, which is exposed by erosion to deeper levels than the dikes in Black Canyon. For example, features such as cusps at the join of the main dike and uncoalesced segments are not exposed in the Black Canyon dike arrays. Parentheses denote terms of Delaney and Pollard (1981) not used in this report.

Figure 4. Longitudinal section of dike tip at location 11 (fig. 1), viewed from above. Internal partings are concentric to the shape of the contact (arrow); pencil (p) is about 10 cm long.

Figure 6. ▶ *A*, Dike segments between locations 2 and 4 (fig. 1) (north is to left); location 2 is the bulbous structure at upper right; location 3 marks site of deflected southern tip of a tabular dike with bulbous structure at location 4 (described in tables 1 and 2) (telephoto view, from a distance of about 0.5 km). ▼ *B*, Curved fissile joints in bulbous structure at location 5; scale shown by figure (and shadow) at left edge of photograph.

over an outcrop. Dikes commonly show magnetic-polarity reversals along the length of outcrop, which we ascribe to lightning strikes. Magnetic susceptibility measurements on samples of dikes north of Highway 93 suggest that they have one-half to one-third the bulk magnetization of intrusions in the vent area. We found no magnetic anomalies to indicate the presence of multiple dikes or large intrusive masses in the subsurface north of the vent area.

Dike segments in Black Canyon are offset, and the ends of some offset segments overlap. These relations are best exposed in the western array (segments between locations 7 and 11*B*, fig. 1). The cause of offsets between dike exposures was discussed by Campbell and Schenk (1950), and a dike with similar structure at Shiprock, New Mexico, has been studied in detail by Delaney and Pollard (1981; fig. 5).

The tips of adjacent offset and overlapped segments commonly are deflected away from each other, and some tips have different strikes from the overall strike of the dike segment. At location 11, the parabolic tips of two dikes are within a few meters of each other; the segment north of location 11 and its tip both have northwest strikes. However, the segment south of location 11 has a northerly strike on average, but its tip is deflected to the northeast (fig. 1). The north tip of the dike segment between locations 10 and 11*A* is deflected to the northeast from the main north trend of the segment such that the tip trends toward the overlapped south tip of the dike segment between locations 8 and 9 (fig. 1). The two dike tips are separated by 200 m. In contrast, two segments with overall due north trends pinch out at location 11*A*, where the overlapping tips are offset 7.6 m; both these tips have northwest trends. Deflection of the tips probably reflects local stress fields present during intrusion of the dike segments, which are branches of a main intrusion at deeper levels (Delaney and Pollard, 1981; fig. 5).

Only one tabular dike is offset in the middle of its exposed length (about 10 m south of location 8), possibly as a result of late Miocene faulting. However, the dike has no relief above the ground surface, and the displacement is so small (one dike width) that unexposed dike geometry, such as two dike tips connected by a small bulbous swelling, could produce the apparent offset (Delaney and Pollard, 1981).

INTERNAL FEATURES

With the exception of the dike segment at location 13 (fig. 1), which is exposed in roadcuts, the internal characteristics of most dikes are seen in longitudinal section

Figure 7. Fanglomerate incorporation in Black Canyon dike segments. ▶ *A*, Breccia of fanglomerate and dike matrix in margin of dike at location 2 (fig. 1) adjacent to bulbous structure; contact of dike and fanglomerate wall rocks is close to the left edge of photograph (arrow); hammer lies across a mass of fanglomerate matrix and clasts; below hammer are two lozenge-shaped masses of quenched basalt (d); dark spots are anhedral kaersutite megacrysts. ▼ *B*, Detail of fanglomerate-basalt breccia; lower edge of photograph, light-colored fanglomerate clasts in darker matrix of baked sandstone; top of photograph, mixed fanglomerate and basalt with large irregular kaersutite megacrysts.

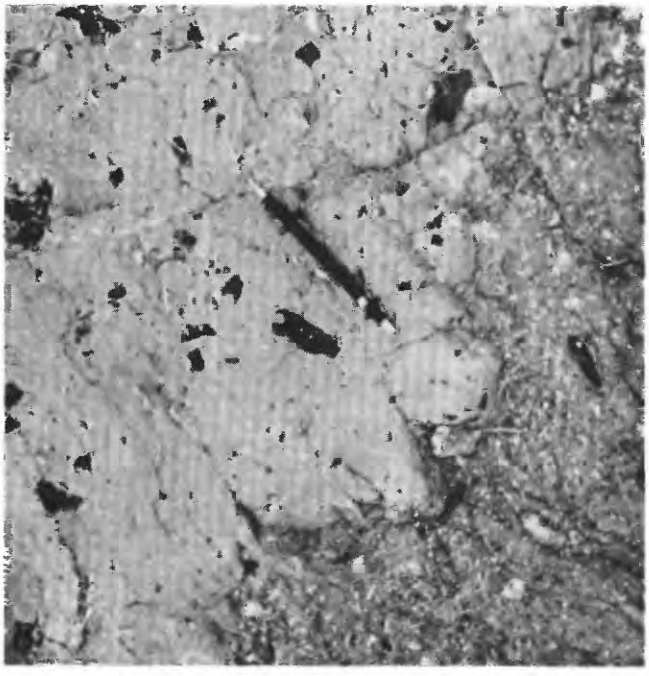

(eroded dike crests); thus, variations along strike can be examined more easily than variations with depth. All the dikes have chilled contact zones. Massive matrix of the contact zones was originally glassy but now is devitrified and mostly altered to clay minerals; the axial parts of dikes more than 100 cm wide have coarser matrix textures. The marginal and internal matrix of all dikes is variably vesicular and locally amygdaloidal, and vesicles locally are flattened parallel to the dike axial plane.

Interior chilled zones are rare and usually occur adjacent to masses of included fanglomerate (fig. 7*A, B*); at one site we observed an internal chilled zone that is parallel to the longitudinal contact and appears unrelated to fanglomerate incorporation. However, the inclusions in this exposure are predominantly centimeter-sized granitic clasts, probably from disaggregated fanglomerate.

The thinnest tabular segments (for example, locations 1 and 12; table 1) and narrow parts of dikes near segment tips are predominantly massive in structure and have very fine grained to fine-grained matrix texture. Matrix plagioclase laths generally are oriented subparallel to each other in a microscopic pilotaxitic texture that is most apparent adjacent to megacryst grains.

Both tabular dike segments and bulbous swellings locally exhibit a variety of joints that probably formed at different stages of dike emplacement or cooling and that interact to form complex patterns. Although some dikes have only massive matrix structure (table 1), the interiors of most dikes contain variably spaced joints that are oriented parallel or subparallel to the axial plane. When, as is common, the joints are closely spaced (1 cm or less), we refer to this matrix structure as "fissile" (tables 1 and 2). Many dikes also exhibit columnar cooling joints, which are perpendicular to the dike walls.

Bulbous swellings have particularly complex internal joint patterns, including irregularly alternating fissile to massive matrix structure and columnar cooling joints. Orientations of joints in the bulbous structures range from horizontal to vertical. Three-dimensional exposures at location 5 (fig. 1) show that the joints that create fissile structure define curved internal surfaces (fig. 6*B*).

STRUCTURE-PARALLEL JOINTS

Zones of massive or fissile matrix structure, formed by closely spaced joints, alternate across the width of many dikes and may vary irregularly along the outcrop length of tabular dike segments. The joint patterns in these segments locally resemble currents in flowing streams (fig. 8). In most exposures, zone margins are parallel or subparallel to axial planes of the dikes; locally the zones may be symmetrical to the axial plane, but arrangements can change to asymmetrical in a short distance along strike (table 2; fig. 9). Near location 4, we observed flow banding in glassy matrix at the contact between the chilled margin and the next zone inward (zone 2), which contains fissile joints (table 2; fig. 10). We believe that the fissile jointing is inherited from flow banding, which is rarely preserved in the devitrified matrix.

In the dike tip at location 11 (table 1), fissile joint structure parallels the parabolic shape of the tip (fig. 4); this relation is the only one in which fissility lies at a high angle to the axial plane and supports an origin of these joints as shear planes in late-stage flow patterns of the intruding magma.

A few tabular dike segments have three to five regularly alternating massive or fissile zones, but such regular zonations continue along strike for only a few meters. Zones merge gradationally; therefore, recorded zone widths (table 2) are measurements based on arbitrary, but consistently applied, boundary criteria. Zones are numbered for convenience in this discussion: zone 1 is always the chilled contact, and zones 3, 4, or 5 may be axial.

The dike segment between locations 3 and 4 contains three zones that all vary in character along strike (table 2). Near location 3, the dike has a massive contact zone (1), a massive to fissile inner zone (2), and a variably fissile axial zone (3). Near the north end (location 4), zone 2 is variably

Figure 8. Dike having irregularly interspersed massive and fissile matrix zones with stream-flow appearance; view of longitudinal section from above. Width of area depicted is about 100 cm.

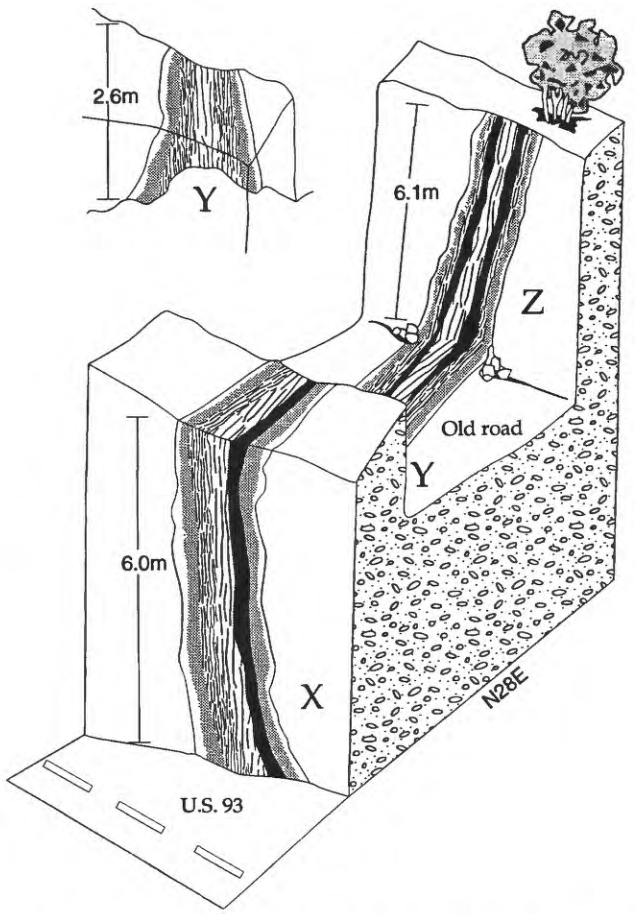

Figure 9. Block diagram of roadcut sections across dike segment at location 13 (fig. 1), showing the gradational variations of structural zones between exposures X, Y, Z (also see table 2 and fig. 11*A*, *B*). Pattern of ovals and dots denotes fanglomerate country rock. Numbered zones correspond to descriptions in table 2. Dike chilled margin (zone 1) is unpatterned, massive zones 2 and 4 are shown in gray and black stipple, respectively. Lined patterns represent finely fissile zones—narrow pattern depicts zone 3, and wide pattern is coarsely fissile zone 5.

fissile and the axial zone is entirely fissile. The dike segment near location 2 contains a fissile axial zone (3), which lies between the dike's central zone (zone 4) and a fine-grained zone (2) inboard of the chilled contact. This fissile axial zone meanders longitudinally in a braided-stream fashion.

The single dike segment at location 13 is exposed by two parallel roadcuts that trend nearly perpendicular to strike of the dike; no other segments have comparable vertical or lateral exposure (figs. 1, 9, 11*A*, *B*). The roadcut sections are labeled X, Y, and Z, from southwest to northeast (figs. 1 and 9); exposures Z and Y are opposite faces of the same roadcut (fig. 9). This dike segment contains as many as five massive and variably fissile zones that range from 3 to 40 cm in width (table 2).

Zones of the dike segment at location 13 vary in width, occurrence, and arrangement between exposures. In exposure Z all the matrix zones are present and arranged symmetrically around the coarsely fissile dike axis (zone 5). However, the massive internal zone (4) is absent in exposure Y (table 2; fig. 9). In exposure X, all zones are present but are arranged asymmetrically—the fissile zone (3) occurs only on the west, and the massive zone (4) only on the east, side of the dike axis. Different asymmetrical arrangements of zones are observed in other dike segments. For example, in the tabular part of the segment be-

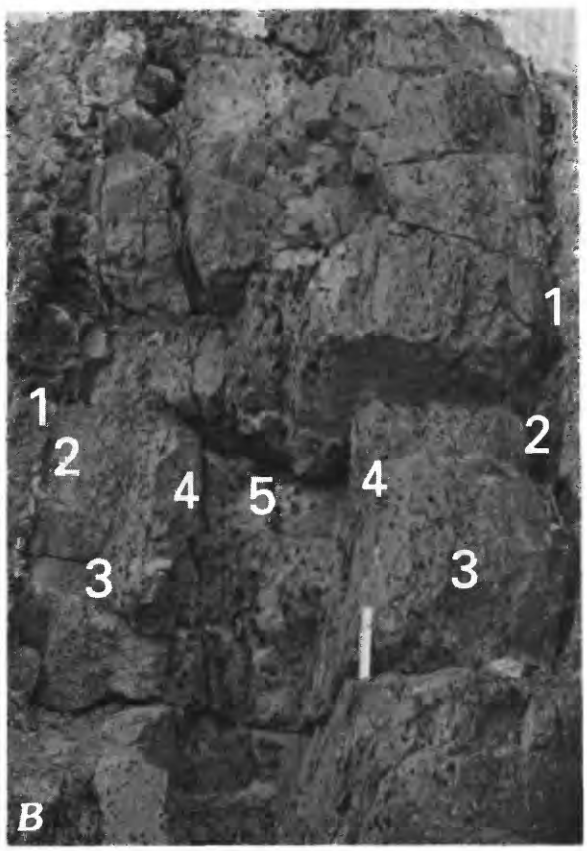

Figure 11. Photographs of dike segment at location 13. *A*, Exposures of dike seen from the south side of U.S. Highway 93. Exposure X is on the modern highway and exposure Z can be seen in old roadcut beyond; exposure Y faces Z in old roadcut (see fig. 9). *B*, Detail of exposure Z showing chilled margins and internal zones (table 2).

Figure 10. Photograph of flow banding in margin of dike at location 4 (fig. 1). Pencil (10 cm length) defines vertical orientation. Long dimension of kaersutite megacryst (left of pencil) is oriented parallel to banding and dike wall. To right (east) of pencil the matrix contains closely spaced fissile joints.

tween locations 5 and 6 and also between locations 10 and 11*A* (fig. 1), a fissile zone 95 cm wide forms the east side, whereas the west side of the dike is massive in structure.

COOLING JOINTS

Columnar cooling joints are common within the dikes. The columns are generally observed on vertical dike walls as polygons 20 to 50 cm across (fig. 12*A*). However, in the dike segment at location 1, interior horizontal to subhorizontal joints with smaller polygonal dimensions occur at the contact between chilled margin and the axial zone. At locations 7, 9, and 11 (fig. 1) small-scale vertical columnar joints occur in the exposed (and eroded) dike crest (fig. 12*B*), suggesting that the top of this outcrop is within a few centimeters of the original upper contact of the dike.

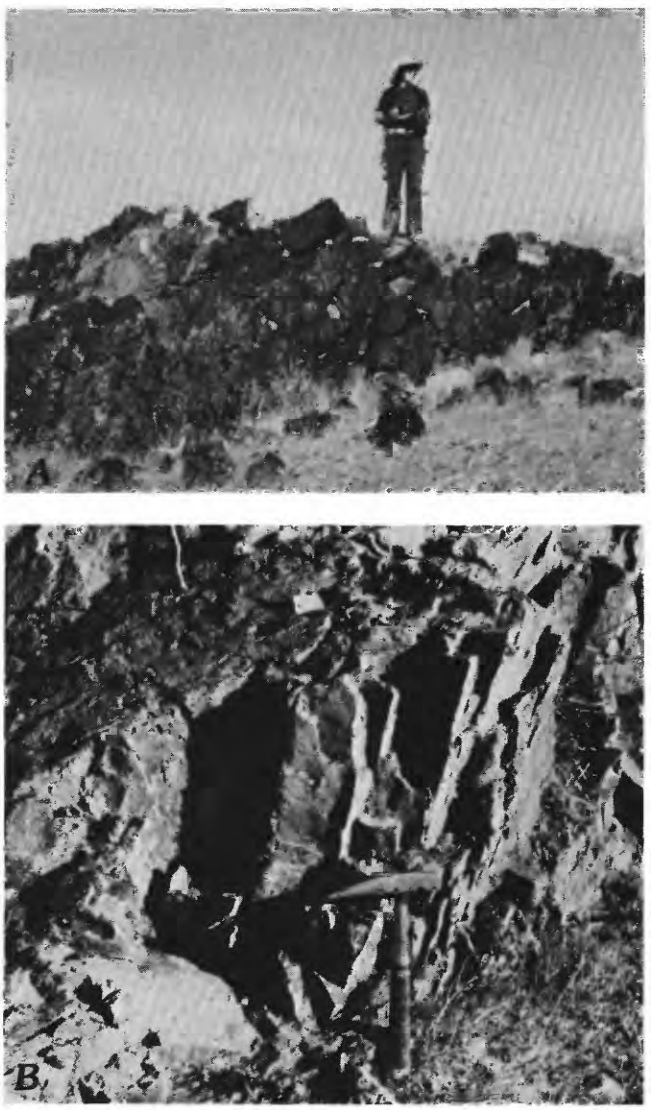

Figure 12. Static cooling joints in Black Canyon dike segments. *A*, Horizontal cooling joints, expressed as polygons on dike wall at location 1 (fig. 1). *B*, Dike at location 7 (fig. 1) showing vertical polygonal cooling joints (photograph is oriented nearly parallel to strike of dike).

INCLUSION SUITE

All segments of Black Canyon dikes, as well as intrusions in the vent area, contain irregular inclusions of shiny black kaersutite. Other minerals observed or reported as inclusions are altered (rarely fresh) olivine, black clinopyroxene, magnetite, milky plagioclase, alkali feldspar (sanidine and anorthoclase; Foland and others, 1980), and quartz. Although usually called "megacrysts," measured kaersutite and pyroxene grains range in size from less than 0.1 mm to as much as 100 mm.

Kaersutite grains normally display cleavage shapes, although many large grains have embayed, irregular outlines (fig. 7*B*). Relic deformation textures identify large, unaltered olivine grains as xenocrysts rather than phenocrysts. Pyroxenes have oval or circular shapes, although a few grains that we analyzed appear euhedral.

Melt and reaction textures are ubiquitous. Plagioclase and quartz grains have spongy margins, probably owing to incipient melting, and many contain cavities with glassy margins, indicating a more advanced stage of melting in the host magma. Locally, large and small kaersutite and clinopyroxene grains have reaction rims, and some kaersutite grains appear to be largely fused. Fused areas in kaersutite grains are altered to fine-grained opaque material, and some enclose small birefringent patches of unfused amphibole. Large amphibole grains commonly show melt-induced fragmentation—grain margins are serrated, and grain splinters, although surrounded by matrix, lie alongside and in optical continuity with the parent grains.

Xenoliths of the inclusion assemblage comprise a mafic and ultramafic suite of altered wehrlite and dunite (±interstitial pargasite), spinel lherzolite with rare unaltered diopside, and pyroxenite, including magnetite- and kaersutite-bearing pyroxenite (A.J. Irving, written commun., 1982). Evidence of a mantle origin for this mafic-ultramafic suite is presented and discussed in following sections.

Felsic rock types among the inclusions are granite, pegmatite, aplite, and various kinds of gneiss. The felsic rocks and some felsic mineral inclusions, such as quartz and possibly K-feldspar, might be derived from lower crustal levels traversed by the magma conduits. However, the felsic inclusions are similar to the mixed gneiss and granite clast types found in the host fanglomerate. Because partly disaggregated fanglomerate masses are observed commonly in the dike exposures, we believe that the fanglomerate is the most probable source of felsic inclusions.

INCLUSION ORIENTATION AND FOLIATION

Some dike segments with abundant mineral and rock inclusions have a foliation that is defined by the preferred

orientation of matrix plagioclase laths, equant sections of tabular inclusions, and long dimensions of flattened vesicles. In tabular dikes this foliation is generally parallel to the axial plane of the dike segment and thus is generally parallel to the planes of fissile joints. Vesicles are rare in fissile zones. In the plane of foliation, plagioclase laths do not define a consistent lineation but generally are oriented tangential to the boundaries of inclusions and vesicles.

Most inclusions, both megacrysts and xenoliths, are tabular. In the dike segment at location 13, the shortest triaxial dimension of inclusion grains is about half of the longest dimension and is oriented approximately perpendicular to both the dike axial plane and the foliation. Regardless of the dike segment dip direction (fig. 13*A*), long dimensions of inclusions are parallel or subparallel to the dip of the dike axial plane. This alignment of inclusion long axes is very prominent in every zone, except the chilled contact zones. Observed inclusion shapes are nearly equant in the plane of foliation and do not form a measurable lineation.

In the dike segment at location 13, all features that parallel the axial plane, including fissile joints, boundaries between fissile and massive matrix, inclusion concentrations, flattening of vesicles, and orientation of the longest dimensions of both matrix minerals and inclusions (table 2) are superimposed, perhaps coincidentally.

INCLUSION DISTRIBUTION PATTERNS

Most of the dike segments contain sparse inclusions with maximum dimensions between 0.5 mm and 100 mm; grains of all sizes are randomly distributed within the two or three most commonly observed patterns of dike structure zonation (table 2, and above). However, three of the dikes that contain a large number of matrix structure zones also contain abundant inclusions that are sorted symmetrically by size with respect to the dike's axial zone. This symmetrical size sorting is observed in dike segments near location 2, in the segment between locations 3 and 4, and in the roadcut sections at location 13 (table 2). In each of these locations, the greatest volume, as well as the largest size of inclusions, is concentrated in axial zones.

Because roadcut sections at location 13 (fig. 1) provided the best exposure of any dike segment, detailed, quantitative measurements of inclusion abundance, mode, size, and shape, were made only at this location. Inclusion abundances for location 13 are listed in table 2 as minimum and maximum mode percent for the three roadcut sections. Abundances listed for other dike segments (table 2) are qualitative estimates, recorded as barren (no inclusions seen), sparse (up to 5 mode percent), abundant (5 to 15 mode percent), and very abundant (greater than 15 mode percent). Inclusion abundances, types, sizes, and size ranges in table 2 are referred to the structural zones as a matter of convenience and should not be regarded as implying a genetic connection.

In the dike segment near location 2, granite and gneiss clasts (fanglomerate derived) are the most abundant inclusions (table 2) and are concentrated in the dike axis (roughly corresponding to zone 4) and the adjacent fissile zone 3. No inclusions were observed in the chilled contact zone, and zone 2 contains only a few small inclusions. Localized between sparsely fissile zone 3 and the axial zone is a pépérite-like breccia, which is composed largely of fanglomerate clasts and lumps of sandy matrix but which also includes anhedral kaersutite megacrysts as much as 30 mm across, olivine grains 10 to 25 mm across, and clasts of nonvesicular dike matrix (fig. 7*A, B*).

Inclusion concentrations and sizes vary along the strike of the dike segment between locations 3 and 4. Near location 3, abundant inclusions occupy both contact and axial zones. A few meters to the north of location 3, inclusions are concentrated only in the axial zone, and the marginal zone is nearly barren. Near location 4, however, inclusions are of lower abundance in all zones, although the axial zone contains a slightly larger volume of inclusions than the other zones (table 2). Close to location 3, inclusions are as much as 70 mm across in the axial zone, and the other zones contain particles less than 25 mm across. Near location 4, inclusions of all sizes are distributed across all the zones.

In the roadcut exposures at location 13 (figs. 1, 9, 11*A, B*), each of the zones contains a range of inclusion sizes. Inclusions are small and sparse in the two outermost zones (≤10 mm in zone 1, <20 mm in zone 2; fig. 13*B*). Zones 3, 4, and 5 have moderate to high inclusion concentrations, which vary within the zones, but abundances are greatest in zone 3 (table 2; fig. 11*B*). The size of the largest inclusions and size ranges of inclusions both increase progressively toward the axial zone (5) (table 2; fig. 13*B*). Although the symmetry of fissile zone 3 and massive zone 4 vary between the three exposures and zone 4 is not present in exposure Y, the symmetrical distribution of inclusion sizes does not change between exposures (table 2; fig. 13*B*).

The field mode (fig. 13*C*) shows that kaersutite is the main mineral inclusion at location 13. Olivine is the next most abundant inclusion but is very subordinate to kaersutite. Variations in megacryst/matrix proportions shown in figure 13*C* (circle with dot) are due entirely to variations in the abundance of kaersutite grains, because other components are either minor or have nearly constant abundance across the dike. These minor constituents are pyroxene, magnetite, plagioclase, alkali feldspar (sanidine and anorthoclase; Foland and others, 1980), and quartz (also see Irving, 1977; Garcia and others, 1980). Lithic fragments of granite, gneiss and peridotite also are present in the dike segment at location 13. Like the mineral constituents, the largest rock fragments also are found in zone 5.

RELATION OF INCLUSIONS AND BULBOUS SWELLINGS

Bulbous swellings in dike segments commonly are associated with high inclusion abundances—particularly near partially incorporated fanglomerate pods. The relation between incorporated fanglomerate and bulbous swellings is exhibited at locations 2, 4, south of location 11 (fig. 1), and in the vent area intrusion pictured in figure 3. The bulbous swelling at location 2 (fig. 7) is continuous with a tabular dike segment that contains gneiss and granite

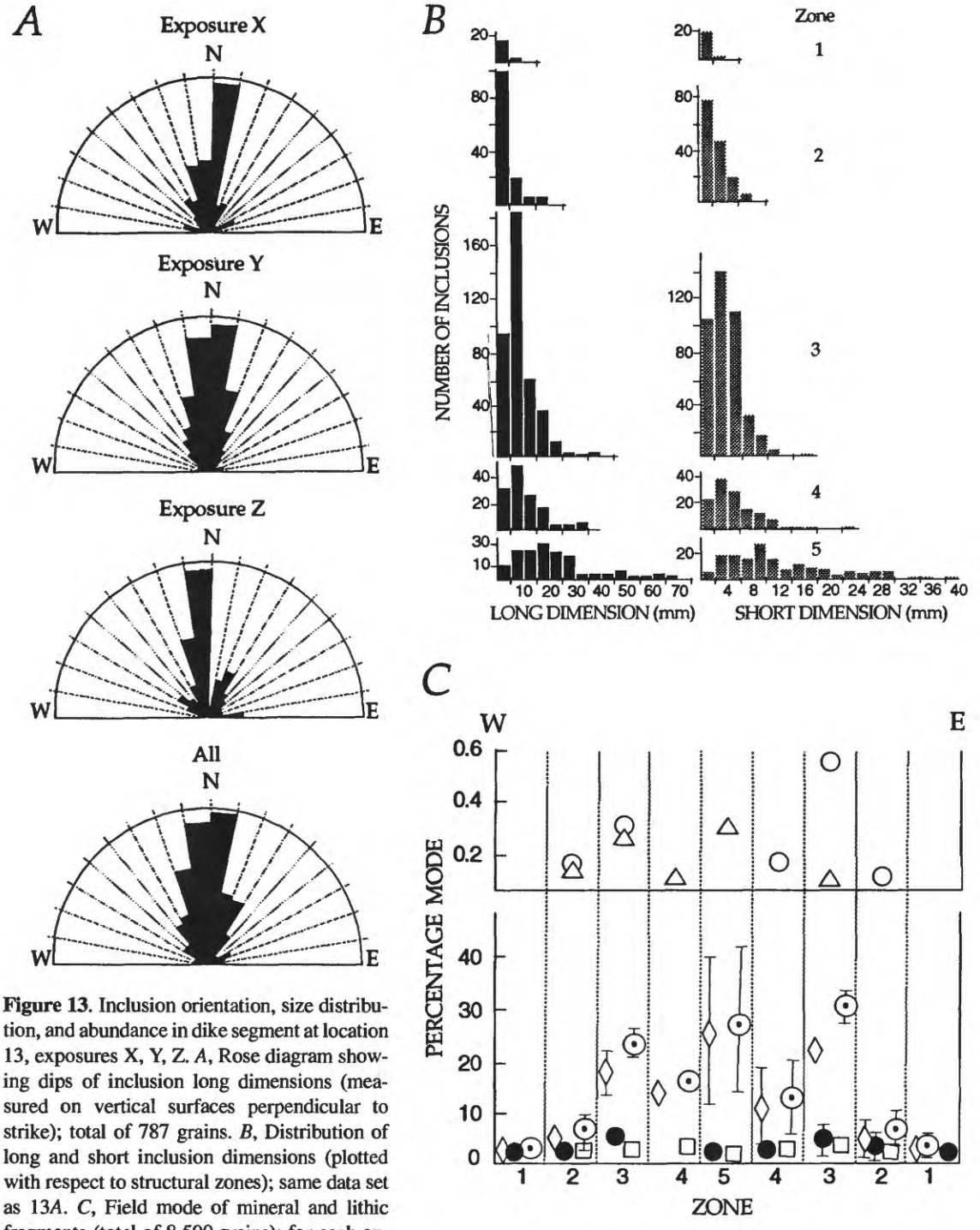

Figure 13. Inclusion orientation, size distribution, and abundance in dike segment at location 13, exposures X, Y, Z. *A*, Rose diagram showing dips of inclusion long dimensions (measured on vertical surfaces perpendicular to strike); total of 787 grains. *B*, Distribution of long and short inclusion dimensions (plotted with respect to structural zones); same data set as 13*A*. *C*, Field mode of mineral and lithic fragments (total of 8,500 grains); for each exposure, modes were counted on two traverses approximately perpendicular to strike of dike; mineral symbols are positioned at average value for six traverses; bars show range of values for all traverses (if greater than size of symbol); mineral symbols: circle with dot, ratio of inclusions to matrix counts given as a percentage; diamond, kaersutite; filled circle, olivine; square, feldspar grains; open circle, clinopyroxene; triangle, ultramafic xenoliths.

clasts concentrated in the axis and contains a marginal breccia of mixed fanglomerate and chilled matrix. At location 4, the dike contact zone contains masses of fanglomerate (fig. 14). Near location 11, the intersection between the tabular part of the dike and a small bulbous swelling (table 1) is very sharp. The tabular part contains a small volume of mixed gneiss clasts, which probably were derived from fanglomerate. Only the large bulbous swelling near location 5 shows no clear relation to incorporation of fanglomerate wall rocks.

COMPOSITION OF DIKES AND INCLUSIONS

PETROGRAPHY AND COMPOSITION OF DIKES

The holocrystalline, aphyric matrix of the Black Canyon dikes comprises plagioclase+altered olivine+altered Ti-augite+magnetite. Samples taken from each structural zone at location 13 have plagioclase laths that range in size from less than 0.1 mm long in the chilled contact zone (zone 1) to 0.5 mm long in the axial zone. Grains of matrix olivine are equant and have a size range similar to the plagioclase, whereas Ti-augite and magnetite grains are smaller than 0.1 mm throughout the dike. Carbonate alteration pervades the matrix; in addition to calcite, patches of analcite, zeolite, and clay minerals are common. Many amygdules and cracks are filled with calcite and analcite.

Major-element analyses and calculated norms in table 3*A* represent three samples (DS-1, -6, and -12) from the axes of thin, massive dike segments with no visible inclusions (dike locations 1, 6, and 12, fig. 1) and one sample (DS-Y2) from the massive zone 2 of exposure Y at location 13 (table 2), which is relatively barren of inclusions. The average bulk compositions of these matrix samples (table 3) are obscured by alteration and the possible presence of microscopic inclusions; also, the original magma compositions may have varied. Samples DS-1, -12, and -Y2 were analyzed untreated (R) and after leaching (L) with dilute HCl to assess the effect of alteration (table 3*A*). Analyses of matrix from Campbell and Schenk (1950) (C-S, table 3*A*), Alibert and others (1986) (A-M-A, table 3*A*), and Daley and DePaolo (1992) (D-D, table 3*A*) are included for comparison. Sample D-D was collected at location 13, and it is likely that the C-S sample was also collected at that site, either from exposure Y or Z of the old roadcut. The dike sampled by Alibert and others (1986) was described as aphanitic and containing rounded kaersutite megacrysts (of unspecified dimensions); it probably is not from the segment exposed in roadcuts at location 13. Normative minerals were calculated for the all samples using program PETCAL (table 3*A*).

Comparison between analyses of leached and untreated dike matrix and examination of the normative minerals in table 3 suggest that the compositions of samples DS-1R, -12R, -Y2R, and -6 are closest to the composition of the Black Canyon juvenile dike magma—probably alkali olivine basalt. The unleached compositions of all four samples have normative olivine; three of them (DS-1R, -12R, -6, as well as A-M-A and D-D) also show nepheline in the norm and thus are alkalic in composition. These compositions agree with the alkalic compositions of matrix clinopyroxene grains, which are difficult to analyze owing to widespread

Figure 14. Mass of fanglomerate (outline) engulfed by dike matrix near dike contact at location 4 (fig. 1). Daypack in lower part of photograph is about 0.5 m in height.

Table 3. Compositions of dike matrix.

[Analyses by X-ray fluorescence, unless otherwise indicated; A.J. Bartel, J.S. Wahlberg, J.E. Taggart, J. Baker, K.C. Stewart, analysts. R, raw, or untreated dike matrix; L, matrix leached in dilute HCl prior to analysis (preparations of treated samples by D. Sorg); —, mineral not present in the norm]

A. Whole-rock major-element analyses.

Sample	DS-1		DS-12		DS-Y2		DS-6	C-S[3]	A-M-A[4]	D-D[5]
	R (2)	L	R (2)	L	R (2)	L	R			
Analyses (weight percent oxide)										
SiO_2 ----	45.0	49.6	44.9	48.5	43.1	47.7	45.6	43.79	46.16	44.30
Al_2O_3 --	15.6	14.5	15.6	14.9	15.2	14.9	15.4	17.84	15.71	14.95
FeO[1] ---	4.59	5.18	5.23	5.60	3.88	4.27	5.82	3.95	—	6.55
Fe_2O_3[2] -	5.05	5.14	4.21	4.38	5.39	6.06	3.73	4.20	10.07	1.82
MgO ---	5.1	5.0	5.0	5.3	5.5	4.8	5.3	9.45	4.62	3.86
CaO ----	9.1	7.1	9.6	6.9	9.7	7.0	9.1	10.44	8.20	8.44
Na_2O ---	4.0	3.3	3.2	2.9	2.6	2.4	3.2	5.30	4.51	3.23
K_2O ----	2.8	2.4	2.8	2.5	1.9	1.8	3.1	1.96	3.22	2.87
TiO_2 ----	2.9	3.3	2.9	3.2	2.8	3.3	3.0	2.48	2.93	2.89
P_2O_5 ----	0.80	0.32	0.79	0.39	0.76	0.22	0.82	0.54	0.92	0.76
MnO ---	0.16	0.16	0.16	0.15	0.15	0.15	0.16	0.04	0.17	0.15
H_2O^+ ---	1.36	1.76	2.80	2.65	2.64	3.06	2.48	3.93		
H_2O^- ---	0.63	1.32	0.47	1.30	2.05	3.15	0.83	2.72	(LI 3.21)	(LI 9.1)
CO_2 ----	1.98	0.03	1.87	0.01	3.00	0.09	1.50	2.99		
Total -	99.07	99.11	99.53	98.68	98.67	98.90	100.04	99.96	99.67	98.81
Normative minerals (weight percent)[6]										
Ap ------	1.95	0.77	1.94	0.95	1.93	0.55	1.99	1.25	2.21	1.96
Il --------	5.79	6.53	5.83	6.41	5.84	6.76	5.98	4.71	0.38	6.11
Mt ------	7.27	7.76	6.47	6.71	5.36	5.06	5.68	5.67	—	2.94
Or-------	17.40	14.77	17.53	15.60	12.34	11.49	19.23	11.58	19.71	18.88
Ab ------	18.42	29.08	18.42	25.91	24.18	21.93	18.379	2.77	27.33	21.67
An ------	17.18	18.39	21.12	21.38	26.59	26.53	19.426	19.10	13.58	19.83
Di-------	19.30	12.56	18.83	9.51	16.23	7.33	17.77	22.70	9.70	17.32
Hy ------	—	7.26	—	11.2	0.04	9.51	—	0.69	—	—
Ol-------	3.09	—	4.30	—	5.25	—	6.08	9.12	5.20	6.53
Ne ------	9.30	—	5.56	—	—	—	5.45	—	6.61	4.74
Q -------	—	2.86	—	2.31	—	7.78	—	—	—	—
Hm -----	0.30	—	—	—	2.22	3.05	—	0.29	10.43	—

[1]Gravimetric determination for samples DS-1, DS-12, DS-Y2, and DS-6, H.M. Neiman, G. Mason, P.R. Klock, C. Stone, S. MacPherson, analysts. (2) designates average of two determinations for unleached (R) samples. Calculation of value for sample D-D given in Daley and DePaolo (1992)

[2]For samples DS-1, DS-12, DS-Y2, Fe_2O_3 value calculated: FeO gravimetric determination subtracted from total Fe determined by X-ray spectrography. For sample A-M-A total Fe is given as Fe_2O_3.

[3]Analysis from Campbell and Schenk (1950); all oxides by gravimetric determination.

[4]Analysis from Alibert and others (1986); authors also report minor and trace element compositions, including rare earth elements. LI, loss on ignition.

[5]Analysis TID-1 from Daley and DePaolo (1992); note that isotopic composition reported under this sample number was determined on an amphibole megacryst (E. Daley, oral commun., 1993). Total given here omits Cr_2O_3 (0.012 weight percent). LI, loss on ignition.

[6]All norms calculated with program PETCAL, written by Richard Koch, U.S. Geological Survey.

alteration (table 4; analytical technique described in table caption). The clinopyroxene grains are augite with high titanium and iron contents (TiO_2, 3.4 to 4.7 percent) and Mg-ratios [Mg/(Mg+ΣFe)] between 0.71 and 0.76.

Unleached samples are rich in CaO (9.1 to 9.7 percent) and samples for which volatiles were determined are also rich in CO_2 (1.9 to 3.0 percent), whereas both these components are reduced significantly in the leached equivalents. Also, Al_2O_3 and Na_2O contents are reduced as much as 1 percent by leaching. All leached samples contain normative hypersthene+quartz and thus appear to be subalkaline. Whether leached or unleached, samples of dike matrix from location 13 (Y2R, Y2L, C-S and D-D) all contain normative hypersthene.

Table 3. Compositions of dike matrix—Continued.

B. Stable isotope compositions of carbonate in dikes, inclusions, and fanglomerate wallrocks.

Sample No.	BC-C1	BC-C2	BC-C3	BC-C4	BC-C5	BC-C6	BC-C7
$\delta^{13}C$[1]	-3.97	-1.74	-5.62	0	+1.45	+0.61	+0.11
$\delta^{18}O$[2]	+34.73	+32.46	+38.58	0	+22.59	+20.79	+22.78
Yield (pct)	62.4	83.3	69.8	0	85.1	91.3	1.0

[1] Analyses by L.D. White, courtesy of I.R. Barnes.
[2] Analyses courtesy of J.R. O'Neill.

Samples:
C1—Fanglomerate 20 m from nearest dike.
C2—Amygdule in dike axis (exposure Z).
C3—Partly assimilated fanglomerate mass in dike.
C4—Kaersutite megacryst.
C5—Tuff breccia.
C6, C7—Amygdules in massive dike, vent area.

We suggest that the subalkaline compositions reflect either removal of important constituents by the leaching or—in the case of location 13—unavoidable contamination by the ubiquitous inclusions, particularly by silicic components. Because the compositions of leached samples change from alkalic character toward compositions incompatible with the modal mineralogy, we suggest that most of the CaO in matrix carbonate was derived from the dike minerals by reaction with near surface waters and was not added by alteration after intrusion. Therefore, removal of carbonate by leaching samples before analysis produces false matrix compositions.

The isotopic compositions of carbon and oxygen in the matrix carbonate (table 3*B*) usually resemble values typical of sedimentary rocks ($\delta^{13}C$ of +1.45 to −1.74; $\delta^{18}O$ of +20.79 to +38.58). One carbonate sample from a partly disaggregated clump of fanglomerate within the dike segment near location 2 (fig. 1) produced a $\delta^{13}C$ of −5.62, which resembles some values of carbonatite and diamond but also overlaps values reported from sedimentary rocks. We suggest that this dike segment is now in equilibrium with ground water isotopic compositions as a result of isotopic exchange during late-stage alteration at the time of crystallization or during later weathering, or both. If any of the carbonate originally had a mantle origin, as suggested by M.O. Garcia (written commun., 1984), it cannot now be discerned.

Basu (1978) determined $^{87}Sr/^{86}Sr$ of 0.70399±.00008 for a leached sample of dike matrix, and Alibert and others (1986) obtained a similar value of 0.703789±.000038; these values resemble Sr-isotopic ratios of most alkali basalts. Foland and others (1980) found a value of 0.70456 for untreated whole rock and a value of 0.70316 for the same rock after leaching with HCl; the Sr-isotopic composition of the soluble fraction resembled that of $CaCO_3$ from amygdules. Foland and others (1980) concluded that these results are consistent with derivation of carbonate from crustal sources, consistent with the near-surface characteristics of stable isotopes that we report.

COMPOSITIONS OF MAFIC INCLUSIONS

Ultramafic and mafic xenoliths and megacrysts of mantle origin are uncommon, but most are found in mafic alkalic intrusions or ejecta (Ross and others, 1954). We determined compositions of mafic megacrysts and minerals from mafic and ultramafic inclusions in the Black Canyon dikes to determine whether the mafic-ultramafic suite derives from the same or a variety of mantle regions.

All analyzed megacrysts but one are kaersutite or clinopyroxene grains, and most are from the roadcut at location 13. Samples from a few other dikes were included for comparison. Most of the clinopyroxene samples are black, glassy, and have irregular shapes. We did not observe any orthopyroxene megacrysts and none are reported in the literature. Two small kaersutite grains (matrix size) were analyzed for comparison with larger grains. From an intrusion in the vent area, we found one olivine megacryst that was fresh enough to analyze.

To test the hypothesis of F.J. Spera (written commun., 1984) that some of the kaersutite particles could be phenocrysts of the dike magma, we also sought amphibole grains that could be identified as euhedral (having regular outlines, uncontrolled by cleavage). We found five candidate euhedral grains during several traverses of every dike segment in the three Black Canyon dike arrays; three of these inclusions proved to be amphibole (EG, table 6) and two are augites. In numerous thin sections, we saw no compositionally zoned amphibole grains, such as those mentioned by F.J. Spera (written commun. 1984).

Mafic to ultramafic xenoliths found in the Black Canyon dikes represent a variety of rock types and have various textural relations:

1. Altered lherzolite xenoliths are light-green granular masses containing relatively fresh chrome-diopside and brown orthopyroxene (tables 4, 5, and 7; see also Irving, 1977; Garcia and others, 1980). Some of the lherzolites contain interstitial kaersutite, and we observed two composite lherzolites with thin kaersutite veins. One analyzed sample (BC-2-21, tables 5 and 6) contains a 1- to 5-mm-wide vein of orthopyroxene+kaersutite.

2. Red-brown altered olivine clusters (wehrlitic xenoliths) are altered olivine grains poikilitically enclosed by black Ti-clinopyroxene±amphibole (possibly "pargasite wehrlite" of Irving, 1977). Analyses of clinopyroxene and amphibole from wehrlitic xenoliths are in tables 4 and 7, respectively.

3. Al-augite pyroxenites are granular masses that may also contain orthopyroxene and intergrown kaersutite (Irving, oral commun., 1982). We found small pyroxenite xenoliths but were unable to collect or analyze them.

4. Kaersutite grains poikilitically enclose biotite and apatite grains (KPA, tables 6 and 9), in clusters that could represent xenoliths or glomerophenocrysts. KPA aggregates have been reported as glomerophenocrysts from other xenolith and megacryst localities (for example, Irving, 1974); such intergrowths are a well-known association in veins and (or) pods in both alpine peridotites (Conquéré, 1970; Spray, 1982; Mukasa and others, 1991) and peridotite xenoliths in basalts (Wilshire and Trask, 1971; Best, 1974, 1975; Wilshire and others, 1980).

Complete analyses of kaersutites from the dike segment at location 13 have been published previously (table 8) by Campbell and Schenk (1950), Garcia and others (1980), and Boettcher and O'Neill (1980). Irving (1977), Basu (1978), and Foland and others (1980) published partial analyses of a wide range of megacrysts.

OLIVINE

The granular olivine cluster analyzed (table 9) lacks strain lamellae and probably is a recrystallized megacryst. Because of the widespread alteration, ours is the only olivine analyzed from the Black Canyon dikes. The forsterite content of this sample (Fo_{79}; CaO, 0.35 percent) is near the middle of the range (Fo_{70} to Fo_{84}) reported for olivine megacrysts from alkalic lavas in the western United States and worldwide (Binns and others, 1970; Wilkinson, 1975; Fodor, 1978). However, chemical compositions of xenocryst and phenocryst olivines may be indistinguishable; for example, Wilkinson (1975) reported an alkalic sill that contains an olivine xenocryst with $Fo_{77.9}$ to $Fo_{83.9}$, Ti-augite-bearing peridotite nodules with olivine compositions of $Fo_{76.4}$ to $Fo_{85.9}$, and groundmass olivine of $Fo_{77.8}$ to Fo_{86}.

PYROXENE

Peridotite xenoliths of the inclusion suite contain both diopsidic and augitic clinopyroxenes, whereas all clinopyroxene megacrysts are Ti-augites (table 4). In the pyroxene quadrilateral (fig. 15), clinopyroxenes from lherzolite xenoliths in the Black Canyon dikes are diopside to subcalcic diopside. Compositions of poikilitic clinopyroxene grains in wehrlitic xenoliths overlap the megacryst compositions, and both the poikilitic grains and the clinopyroxene megacrysts have trends from diopside toward Fe-enriched augite (fig. 15; table 4).

The distinction between lherzolite and wehrlite clinopyroxene compositions persists for important nonquadrilateral components (table 4). Diopsides from lherzolite are chrome-rich (0.46 to 1.1 percent Cr_2O_3) and low in Ti and Al (0.31 to 0.71 percent TiO_2; 4.3 to 6.1 percent Al_2O_3). Poikilitic clinopyroxene grains have low chrome contents (0.13 to 0.16 percent Cr_2O_3) but high Ti and Al contents (TiO_2, 0.71 to 2.0 percent; Al_2O_3, 4.5 to 8.1 percent). In contrast, chrome contents of clinopyroxene megacrysts are moderate (0.30 to 0.57 percent Cr_2O_3), and ranges of Ti and Al values are relatively restricted (TiO_2, 1.7 to 2.0 percent; Al_2O_3, 7.2 to 8.0 percent). The large compositional range of Ti and Al in poikilitic clinopyroxenes fills the gap between the compositions of megacrysts and grains in lherzolite.

Roden and Shimizu (1989) reported an even larger range in TiO_2 content (1.9 to 4.4 percent) for clinopyroxene grains from xenoliths with refractory compositions (Group I) collected from Black Canyon ("Hoover Dam")

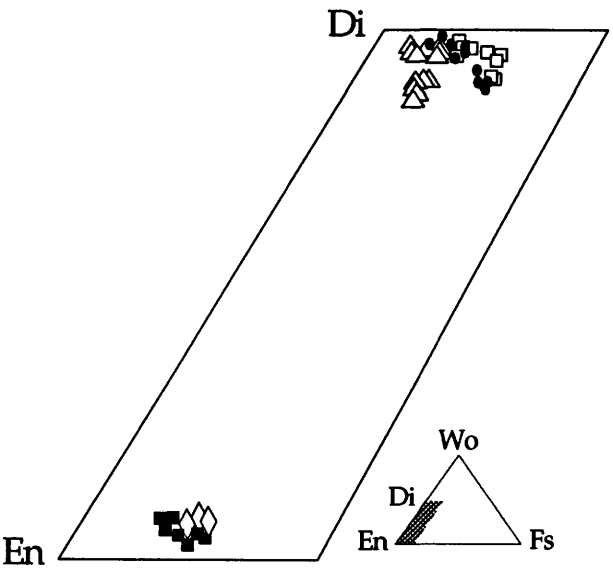

Figure 15. Quadrilateral components of pyroxene minerals in the Black Canyon dikes (calculated values of Wollastonite (Wo), Ferrosilite (Fs), and Enstatite (En); data from tables 4 and 5); shaded area shows location of plot volume between En and Di (Diopside) in pyroxene composition triangle. Mineral symbols: dots, clinopyroxene megacrysts; triangles, clinopyroxene in lherzolite; open squares, poikilitic clinopyroxene in wehrlitic xenoliths; filled squares, orthopyroxene in lherzolite; diamond, orthopyroxene in vein of composite xenolith sample BC-2-21 (table 5).

Table 7. Compositions of amphibole (pargasite) in xenoliths of Black Canyon dikes.

	Poikilitic amphibole in wehrlitic xenoliths (D)												
Sample No.	D1A1	D1A2	D1A3	D1A4	D1A5	D5A1	D5A2	D5A3	D5A4	D5A5	D5A6	D5A7	D5A8
Analyses (weight percent oxide)													
SiO_2	43.0	43.2	43.4	43.4	43.6	43.4	43.3	43.4	41.9	41.8	41.4	41.6	41.1
Al_2O_3	14.1	14.0	14.1	14.0	14.1	13.6	13.5	13.4	13.7	13.6	13.6	13.8	13.6
$FeO^{tot\ 1}$	7.0	6.1	6.6	6.6	6.5	7.3	7.2	7.2	7.2	7.1	7.1	7.2	7.1
MgO	15.7	16.0	15.9	16.0	16.0	15.4	15.5	15.5	15.8	15.8	15.6	15.6	15.8
CaO	11.6	11.8	11.7	11.8	11.7	11.8	11.7	11.8	11.7	11.7	11.6	11.6	11.5
Na_2O	2.9	2.8	2.8	2.9	2.8	2.6	2.6	2.6	2.7	2.6	2.7	2.6	2.7
K_2O	1.2	1.2	1.2	1.2	1.2	1.3	1.3	1.3	1.3	1.3	1.3	1.3	1.3
TiO_2	2.8	2.9	2.9	2.8	2.8	3.1	3.1	3.1	3.0	3.1	3.0	3.1	3.1
Cr_2O_3	0.25	0.24	0.23	0.25	0.24	0.56	0.74	0.66	0.72	0.78	0.99	0.54	0.74
Total	98.55	98.24	98.83	98.95	98.94	99.06	98.94	98.96	98.02	97.78	97.29	97.34	96.94
Mg ratio= Mg/(Mg+SFe)	.80	.82	.81	.81	.81	.79	.80	.79	.80	.80	.80	.79	.80
Amphibole structural formula—23 oxygens													
Si	6.15	6.18	6.18	6.18	6.19	6.19	6.18	6.20	6.06	6.06	6.04	6.06	6.02
Al^{IV}	1.85	1.82	1.82	1.82	1.81	1.81	1.82	1.80	1.94	1.94	1.96	1.94	1.98
Al^{VI}	0.53	0.54	0.54	0.52	0.55	0.48	0.46	0.45	0.40	0.39	0.38	0.43	0.37
$Al^{tot\ 2}$	2.38	2.36	2.36	2.34	2.36	2.29	2.28	2.25	2.34	2.33	2.34	2.37	2.35
Fe^{II}	0.84	0.73	0.79	0.78	0.77	0.87	0.86	0.86	0.87	0.86	0.87	0.88	0.87
Mg	3.35	3.41	3.37	3.39	3.39	3.27	3.30	3.30	3.41	3.41	3.39	3.38	3.45
Ti	0.30	0.31	0.31	0.30	0.30	0.33	0.33	0.33	0.33	0.34	0.33	0.34	0.34
Cr	0.028	0.027	0.026	0.028	0.027	0.063	0.084	0.074	0.082	0.089	0.114	0.062	0.086
Ca	1.78	1.81	1.78	1.80	1.78	1.80	1.79	1.81	1.81	1.82	1.81	1.81	1.80
Na	0.80	0.78	0.77	0.80	0.77	0.72	0.72	0.71	0.76	0.73	0.76	0.73	0.76
K	0.22	0.22	0.22	0.22	0.22	0.24	0.24	0.24	0.24	0.24	0.24	0.24	0.24
Papike A/R[3]	A	A	A	A	A	A	A	A	A	A	A	A	A

Table 7. Compositions of amphibole (pargasite) in xenoliths of Black Canyon dikes—Continued.

Sample No.	Interstitial amphibole in lherzolite (L)										
	LA1	LA2	LA3	LA4	LA5	LA6	LA7	LA8	LA9	LA10	LA11
Analyses (weight percent oxide)											
SiO_2	42.1	42.1	42.0	42.1	41.9	41.9	42.1	42.4	42.3	42.3	42.2
Al_2O_3	14.9	15.0	15.0	14.8	14.8	14.8	15.0	14.8	14.9	14.7	14.9
$FeO^{tot\,1}$	6.2	6.1	6.2	6.2	6.2	6.1	6.1	6.2	6.2	6.1	6.2
MgO	15.7	15.7	15.7	15.8	15.6	15.7	15.6	15.6	15.6	15.6	15.7
CaO	11.7	11.8	11.7	11.8	11.8	11.7	11.8	11.7	11.8	11.8	11.7
Na_2O	2.7	2.6	2.7	2.6	2.6	2.7	2.6	2.6	2.7	2.6	2.7
K_2O	1.3	1.3	1.3	1.3	1.3	1.3	1.3	1.3	1.3	1.3	1.3
TiO_2	3.3	3.3	3.3	3.3	3.3	3.2	3.3	3.2	3.3	3.2	3.3
Cr_2O_3	0.74	0.74	0.71	0.69	0.74	0.73	0.68	0.73	0.74	0.78	0.70
Total	98.64	98.64	98.61	98.59	98.24	98.13	98.48	98.53	98.84	98.38	98.70
Mg ratio= Mg/(Mg+SFe)	.82	.82	.82	.82	.82	.82	.82	.82	.82	.82	.82
Amphibole structural formula—23 oxygens											
Si	6.02	6.01	6.00	6.02	6.01	6.02	6.02	6.06	6.03	6.06	6.02
Al^{IV}	1.98	1.99	2.00	1.98	1.99	1.98	1.98	1.94	1.97	1.94	1.98
Al^{VI}	0.53	0.54	0.53	0.51	0.52	0.52	0.55	0.55	0.54	0.54	0.53
$Al^{tot\,2}$	2.51	2.53	2.53	2.49	2.51	2.50	2.53	2.49	2.51	2.48	2.51
Fe^{II}	0.74	0.73	0.74	0.74	0.74	0.73	0.73	0.74	0.74	0.73	0.74
Mg	3.34	3.34	3.34	3.37	3.34	3.36	3.32	3.32	3.32	3.33	3.34
Ti	0.35	0.35	0.36	0.36	0.36	0.35	0.36	0.34	0.35	0.34	0.35
Cr	0.084	0.083	0.080	0.078	0.084	0.083	0.077	0.082	0.083	0.088	0.079
Ca	1.79	1.81	1.79	1.81	1.82	1.80	1.81	1.79	1.80	1.81	1.79
Na	0.75	0.72	0.75	0.74	0.72	0.75	0.72	0.72	0.75	0.72	0.74
K	0.24	0.24	0.24	0.24	0.24	0.24	0.24	0.24	0.24	0.24	0.24
Papike A/R[3]	A	A	A	A	A	A	A	A	A	A	A

[1]Total Fe expressed as FeO.
[2]Total Al is a plotting parameter in figure 16*A*.
[3]Analysis accepted (A) or rejected (R) by Papike and others (1969) screen for amphibole probe analyses. All "R" analyses listed were rejected on the basis of one criterion and are indistinguishable from "A" analyses.

Table 8. Published compositions of Black Canyon kaersutite megacrysts.

[n.d., not determined; —, not calculated]

Sample No.	C/S[1]	BC-2-24[2]	1[3]	1349243[3]	106434[3]	HD-1[4]	HD-2[4]	HD-3[4]
				Analyses (weight percent oxide)				
SiO_2	41.46	40.3	40.46	40.55	40.36	40.1	39.5	40.2
Al_2O_3	14.24	14.3	13.77	14.59	14.35	14.2	14.1	14.1
Fe_2O_3	3.32	n.d.	n.d.	n.d.	n.d.	n.d.	n.d.	n.d.
FeO	5.70	n.d.	n.d.	n.d.	n.d.	n.d.	n.d.	n.d.
FeO^{tot}[5]	8.69	8.3	8.98	8.63	8.69	7.9	9.7	8.3
MgO	13.68	14.0	13.00	13.74	13.58	14.3	13.2	14.0
CaO	11.62	11.0	11.32	11.03	10.93	11.4	11.5	11.5
Na_2O	2.29	2.6	2.51	2.53	2.47	2.5	2.6	2.6
K_2O	1.72	2.0	1.95	1.96	2.00	1.9	1.9	1.9
TiO_2	5.70	5.7	5.73	5.78	5.49	5.7	5.5	5.6
MnO	0.08	0.1	n.d.	0.14	n.d.	0.14	0.16	0.13
Cr_2O_3	n.d.	0.1	n.d.	n.d.	n.d.	0.19	0.03	0.03
Total	99.81	98.4	97.85	99.03	97.96	98.33	98.19	98.36
Mg ratio= Mg/(Mg+SFe)	.74	.75	.72	.74	.74	.76	.71	.75
				Amphibole structural formula—23 oxygens				
Si	5.93	5.86	5.94	5.87	5.90	5.84	5.82	5.86
Al^{IV}	2.07	2.14	2.06	2.13	2.10	2.16	2.18	2.14
Al^{VI}	0.33	0.32	0.33	0.36	0.38	0.27	0.26	0.28
Al^{tot}[6]	2.40	2.46	2.39	2.49	2.48	2.43	2.44	2.42
Fe^{II}	1.04	1.01	1.10	1.04	1.06	0.96	1.19	1.01
Mg	2.92	3.04	2.84	2.96	2.96	3.10	2.90	3.04
Mn	0.10	0.01	—	0.02	—	0.02	0.02	0.02
Ti	0.61	0.62	0.63	0.63	0.60	0.62	0.61	0.61
Cr	—	0.01	—	—	—	0.02	0.00	0.00
Ca	1.78	1.71	1.78	1.71	1.71	1.78	1.81	1.80
Na	0.64	0.73	0.72	0.71	0.70	0.70	0.74	0.73
K	0.31	0.37	0.36	0.36	0.37	0.35	0.36	0.35
Papike A/R[7]	A	A	R	A	A	A	R	R

[1]Campbell and Schenk (1950): wet-chemical analysis of kaersutite megacryst. Data are presented as anhydrous and FeO^{tot} calculated for comparison with microprobe analyses. Total calculated using values for FeO and Fe_2O_3.

[2]Boettcher and O'Neill (1980): microprobe analysis of kaersutite megacryst.

[3]Garcia and others (1980): microprobe analyses of three kaersutite megacrysts.

[4]A.J. Irving (1982) written commun.: microprobe analyses of kaersutite megacrysts.

[5]Total Fe expressed as FeO.

[6]Total Al values for comparison with those in tables 6–7 and plotted in figure 16*A*; these data are not plotted.

[7]Analysis accepted (A) or rejected (R) by Papike and others (1969) screen for amphibole probe analyses. All "R" analyses listed were rejected on the basis of one criterion and are indistinguishable from "A" analyses.

dikes. These values are mostly higher than the highest TiO_2 compositions found by us, either for clinopyroxene megacrysts or clinopyroxene in xenoliths. Roden and Shimizu (1989) also show high contents of strontium and rare earth elements (REE) in clinopyroxenes with REE patterns that are variably enriched or depleted in light rare earth elements (LREE) compared to heavy rare earth elements (HREE).

All clinopyroxenes in table 4 have compositions characteristic of high-pressure origin, notably high values of Ca-Tschermak's molecule: 15 to 19 percent in diopsides, 13 to 24 percent in poikilitic grains of wehrlite, and 16 to 27 percent in megacrysts. The poikilitic clinopyroxenes have compositions intermediate between Cr-diopside and augite megacrysts (table 4).

Orthopyroxene compositions show less variation (table 5; fig. 15) than clinopyroxene. Orthopyroxene grains intergrown with kaersutite in the vein of lherzolite xenolith BC-2-21 are slightly richer in Fe and poorer in Cr than grains from other lherzolite xenoliths. TiO_2 contents of orthopyroxenes in the three lherzolite samples (table 5) range from 0.08 to 0.37 percent, and orthopyroxene in the vein of sample BC-2-21 (table 5) has a TiO_2 content within this range (0.17 percent).

Table 9. Compositions of phlogopite and olivine.

[n.d., not determined]

	Phlogopite grains (P) intergrown with kaersutite and apatite in kaersutite-phlogopite-apatite cluster (KPA)							Olivine megacryst (OM)
Sample No.	KPA-P1	KPA-P2	KPA-P3	KPA-P4	KPA-P5	KPA-P6	KPA-P7	OM
	Analyses (weight percent oxide)							
SiO_2	35.3	35.1	35.3	35.1	35.0	35.0	35.0	38.9
Al_2O_3	15.7	15.8	15.6	15.8	15.8	15.6	15.6	n.d.
FeO^{tot} [1]	16.3	16.3	16.3	16.5	16.4	16.3	16.2	19.4
MgO	11.4	11.4	11.4	11.4	11.3	11.3	11.3	41.5
CaO	0.15	0.15	0.14	0.14	0.16	0.15	0.13	0.32
Na_2O	0.78	0.82	0.77	0.77	0.77	0.76	0.76	n.d.
K_2O	8.6	8.7	8.6	8.7	8.7	8.6	8.6	n.d.
TiO_2	9.8	9.7	9.7	9.8	9.8	9.8	9.9	n.d.
MnO	0.15	0.14	0.14	0.14	0.14	0.14	0.13	0.24
Cr_2O_3	0.031	0.031	0.033	0.025	0.032	0.026	0.030	n.d.
NiO	n.d.	n.d.	n.d.	n.d.	n.d.	n.d.	n.d.	0.12
F	0.004	0.000	0.001	0.001	0.001	0.001	0.002	n.d.
Total	98.22	98.14	97.98	98.38	98.10	97.68	97.65	100.48
Mg ratio= Mg/(Mg+SFe)	.56	.56	.56	.55	.55	.55	.55	$^2Fo_{79}$
Na_2O/K_2O	.089	.094	.090	.088	.088	.088	.088	n.d.
Structural formulae	**22 oxygens**							**4 oxygens**
Si	5.2	5.2	5.2	5.1	5.1	5.2	5.2	1.0
Al^{tot} [3]	2.7	2.7	2.7	2.7	2.7	2.7	2.7	n.d.
Fe^{II}	2.0	2.0	2.0	2.0	2.0	2.0	2.0	0.42
Mg	2.5	2.5	2.5	2.5	2.5	2.5	2.5	1.6
Mn	0.02	0.02	0.02	0.02	0.02	0.02	0.02	0.005
Ni	n.d.	n.d.	n.d.	n.d.	n.d.	n.d.	n.d.	0.002
Ti	1.1	1.1	1.1	1.1	1.1	1.1	1.1	n.d.
Cr	0.004	0.004	0.004	0.003	0.004	0.003	0.003	n.d.
Ca	0.02	0.02	0.02	0.02	0.02	0.02	0.02	0.008
Na	0.22	0.23	0.22	0.22	0.22	0.22	0.22	n.d.
K	1.6	1.6	1.6	1.6	1.6	1.6	1.6	n.d.
F	0.001	0.000	0.000	0.000	0.000	0.000	0.001	n.d.

[1]Total Fe expressed as FeO.
[2]Fo=Mg ratio x 100.
[3]Total aluminum ions.

M.F. Roden (written commun., 1992) has found a much smaller range of TiO_2 (0.06 to 0.21 percent) and Al_2O_3 values for orthopyroxene grains in analyses of Black Canyon xenoliths than we report (we found 3.2 to 5.0 percent Al_2O_3 in the three samples, whereas Roden found 4.4 to 5.6 percent Al_2O_3). We also found higher values of MgO (as much as 33.4 percent, compared to 32.8 found by Roden). For other oxides, Roden's orthopyroxene data have larger ranges that completely overlap the values reported in table 5. However, compared to either set of xenolith data, orthopyroxene grains in the kaersutite vein of xenolith BC-2-21 are higher in FeO (7.0 percent).

AMPHIBOLE

We analyzed 76 amphibole samples from xenoliths and megacrysts (table 6) with an electron microprobe. To avoid bias in favor of large or small grains or of position relative to the dike walls, hand samples were taken at measured intervals from exposures X, Y, and Z (location 13). Whole or parts of 58 megacrysts were selected randomly from these samples for the analyses. In polished thin sections made from samples of zones 3, 4, and 5, all mafic mineral grains were traversed with the electron beam to test the possibility of compositional zoning. All analyzed amphiboles were homogeneous.

Interstitial amphiboles in peridotite xenoliths (table 7) are pargasite (low Ti-values and high Mg ratios). All other amphibole samples from xenoliths, including those in the KPA cluster (fig. 16*A* and *B*; table 6), are kaersutite (definition of Leake, 1978) with at least 0.5 Ti atoms per formula unit. Black Canyon amphibole megacrysts form a chemically coherent group (figs. 16*A* through *C*). Compositions from samples of apparently euhedral megacrysts and those of matrix-size grains in thin sections (AM7, table 6) are well within the compositional range of plotted parameters for all amphibole megacrysts.

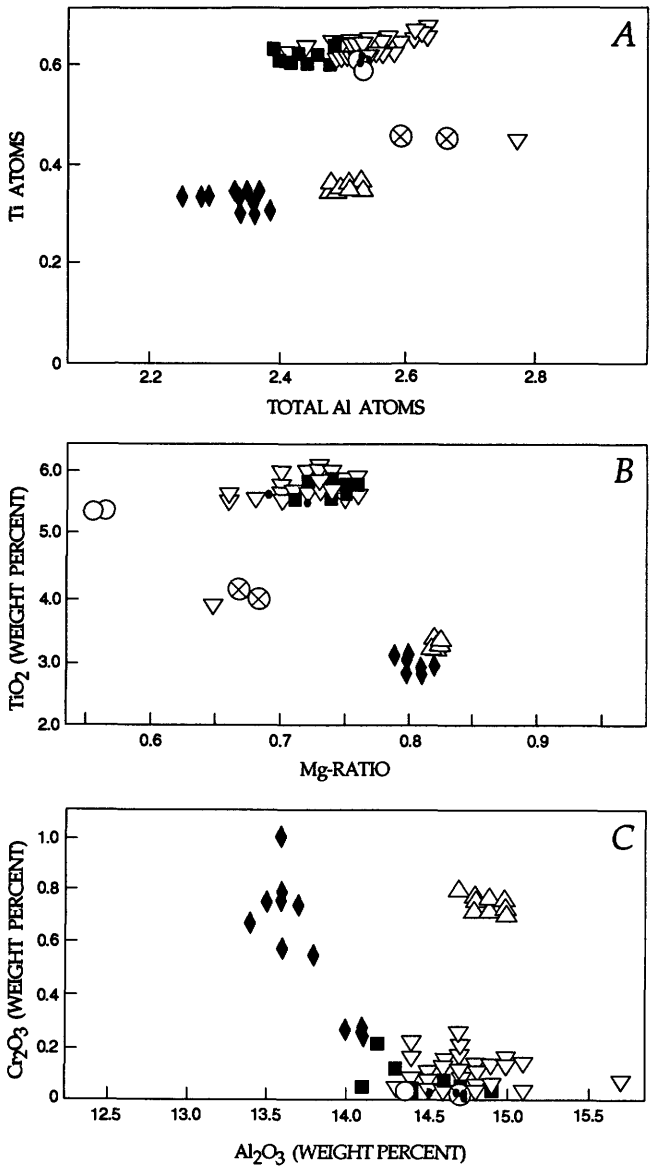

Figure 16. Amphibole compositional variations. *A*, plot of structural Al and Ti (after Best, 1974, 1975). *B*, Mg-ratio and TiO_2. *C*, variations of Cr_2O_3 and Al_2O_3. Symbols: inverted triangle, megacrysts, including supposedly euhedral grains and matrix-sized grains; circle with x, fused grain (altered megacryst); filled diamond, kaersutite in wehrlitic xenoliths; large open circle, kaersutite in kaersutite-phlogopite-apatite (KPA) aggregate; small filled dot, vein; upright triangle, lherzolite xenoliths.

Similar data plotted by Best (1974) show that amphibole megacryst compositions worldwide have Ti values of 0.3 to 0.7 atoms per formula unit and Al values from 1.9 to 2.8 atoms per formula unit (fig. 16*A*). Compositions of megacrysts from Grand Canyon localities alone occupy nearly the entire range of amphibole megacryst Ti values (Best, 1974). By comparison, all but three Black Canyon kaersutite analyses fall into a restricted compositional range: Ti from 0.61 to 0.67 and Al from 2.4 to 2.6 atoms per formula unit (fig. 16*A*). Kaersutite grains from the vein of xenolith BC-2-21 (table 6; small dots, fig. 16*A* through *C*) have compositions indistinguishable from most amphibole megacrysts.

Figure 16*B* displays Mg ratio plotted against TiO_2 content (as weight percent) for all analyzed Black Canyon amphibole samples. Of the 61 megacryst compositions plotted, most are anhedral grains or cleavage fragments; however, three were selected because they appeared to be euhedral (table 6; fig. 16*B*). All megacryst samples but one have Mg ratios between 0.64 and 0.76. TiO_2 values for most megacrysts are bracketed between 5.5 and 6.0, although analyses of Black Canyon megacrysts from the literature range to as much as 6.3 TiO_2 (table 8).

Three megacryst samples plotted in figure 16*B* have TiO_2 values much lower than the dominant range (4.8 to 5.0) and markedly high contents of Fe. Two of these low-Ti megacrysts (circle with x, figs. 16*A* through *C*) are parts of a single fused grain; thus, the Mg ratios of 0.67 and 0.68, and TiO_2 values of about 4.0 weight percent probably represent compositions that were altered by reaction in the magma. The other megacryst with low contents of Ti and Mg is from the contact zone; it has very high Al_2O_3 and also may have undergone partial melting, dissolution, or reaction.

Amphibole grains intergrown with phlogopite and apatite (KPA, table 6; large open circles, figs. 16*A* through *C*) have Ti values and contents of Al_2O_3 and Cr_2O_3 similar to megacrysts, but are distinguished by markedly low Mg ratios (0.55 to 0.56) compared to megacrysts. Therefore, the KPA grains do not resemble interstitial pargasite from lherzolite xenoliths (filled diamonds, figure 16*A* through *C*), which have high Cr_2O_3 and Al_2O_3 relative to megacrysts.

Megacrysts vary more widely than other amphiboles in Al_2O_3 content (14.3 to 15.7; fig. 16*C*), at low values of Cr_2O_3 (0.20 to less than 0.01). The alumina contents of poikilitic amphibole in wehrlitic xenoliths are lower and more restricted than megacrysts, but the Cr_2O_3 values vary from slightly higher than megacrysts (0.23) to ones higher than lherzolite amphiboles (0.99).

Figure 17 shows the compositions of amphibole megacrysts plotted against position in the dike segment at location 13 (table 1). The average compositions of three anhedral and two euhedral kaersutite grains from other

dikes of the swarm are included for comparison. The megacrysts are essentially uniform in Al and Cr across the zones of the dike, and all other compositional variations show no correlation with position in the dike.

One small amphibole grain in the contact zone is markedly different from the bulk of megacrysts in Al and Ti values and Mg ratio. However, other zones contain amphiboles with similar low Mg ratios—all these grains are fused and probably were altered by reaction with the magma, as discussed above. Other than this grain, Ti- and Al-values show little variation across the width of the dike. Chrome contents and Mg ratios vary most widely in zones 3 and 4, probably owing to the larger number of analyzed grains, which reflects the greater abundance of grains in these zones (fig. 13*B*).

Basu (1978) determined K, Rb, Sr, and Ba contents and Sr-isotopic ratios for a Black Canyon kaersutite megacryst and part of the surrounding dike matrix. The potassium content determined by Basu (1978) (1.6 weight percent K_2O) is within the range of microprobe determinations in our study (range 1.3 to 2.0 weight percent K_2O) for megacrystal and xenolithic kaersutites. A kaersutite megacryst from Black Canyon analyzed by Irving and Frey (1984) is relatively enriched in LREE compared to HREE and has a chondrite-normalized LREE/HREE value of about 3.0. Sr-isotopic ratios for two Black Canyon kaersutite megacrysts are 0.70275±0.00005 (Basu, 1978) and 0.70273 (Foland and others, 1980). These values from different laboratories are in remarkable agreement and are comparable to the ratios of mantle-derived kaersutites worldwide (Basu, 1978). An amphibole analyzed by Daley and DePaolo (1992) has a ε_{Nd} value of +6.4 and Sr-isotopic ratio of 0.70293, which is slightly higher than those of the megacrysts analyzed by Basu (1978) and Foland and others (1980), but much lower than values for dike matrix.

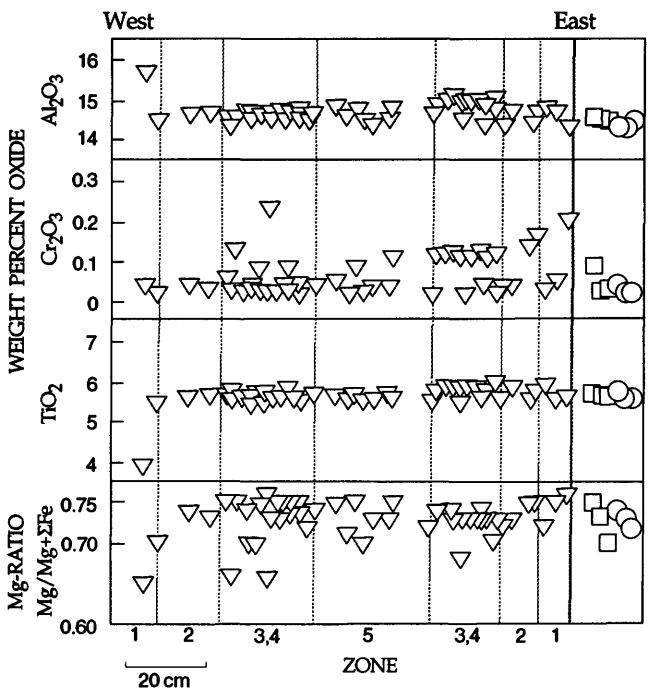

Figure 17. Variations of amphibole (kaersutite) compositions plotted against distance across the width of the dike at location 13 for exposures X, Y, Z; compared to amphibole megacrysts from other Black Canyon dikes and grains that appeared euhedral. Symbols: inverted triangles, kaersutite megacrysts from location 13; squares, megacrysts from other dikes; circles, euhedral grains. Abscissa location of symbols for other dikes is not significant.

OTHER MINERALS

Seven analyzed phlogopite flakes (table 9) in the KPA cluster (table 6) have constant TiO_2 contents of 9.8 weight percent and Mg ratios between 0.39 and 0.55. Thus, all the mica compositions lie within the range reported by Irving (1977) and are similar to those from secondary phlogopites in peridotites (Boettcher and O'Neil, 1980). Although we did not analyze feldspars, some may be of high-pressure origin; for example, Irving (1977) analyzed titanomagnetite and sodic plagioclase (oligoclase-andesine) megacrysts from the dike segment at location 13. Foland and others (1980) reported anorthoclase megacrysts that have a range of $^{87}Sr/^{86}Sr$ between 0.70298 and 0.70396. The higher isotopic ratio of strontium is similar to that determined by Foland (1980) for Black Canyon dike matrix (see above); thus, the anorthoclase could have crystallized from the dike magma under high pressure conditions.

DISCUSSION

FORMATION OF THE BLACK CANYON VENT AREA

Geologic and magnetic mapping indicate that an eruptive center formed at the south end of the Black Canyon dike arrays. Lava flows are absent or are of relatively small volume in the vent area; also, fragments of scoriaceous basalt are rare, and no cinder horizons are interbedded either in fanglomerate or tuff breccia. These observations imply that the volume of magma was too small or conduit pressures were too low to sustain lava fountaining.

Many lines of evidence, such as the mixtures of fanglomerate and rapidly chilled, fragmented magma in the tuff breccia, accretionary lapilli in layered tuff breccia, and pépérite zones in the tuff breccia adjacent to some dikes indicate a wet depositional environment. Therefore, the tuff breccia may be the product of one or more phreatomagmatic eruptions, caused by basaltic magma intrusions into a relatively watery part of the fanglomerate deposit. However, no maar-bed deposits are preserved in

the vent area; therefore, the eruptions were not especially violent.

The tuff breccia, fanglomerate, and tuff-fanglomerate contacts are intruded by dikes and sills; thus, intrusion continued after eruption of the tuff breccia, emplacing multiple intrusions or a large intrusive mass that our magnetic survey indicates must be present at depth. Our field observations show that several distinct dikes with a range of magnetic susceptibilities crop out at the surface; therefore, we conclude that the magnetic source in the vent area consists of many intrusions with variable magnetizations.

Multiple injections of alkalic magma into a small area of venting characterize the process of diatreme formation (Dawson, 1967). Diatremes are very deeply rooted structures with complex internal relations produced by violent eruptions, which are driven by high pressures from deep crustal or upper mantle levels. In the Black Canyon vent area, features such as accretionary lapilli in layered tuff breccia and the steep contacts between eruptive-intrusive units and the country rock in the southern part of the area support a possible origin of the vent area as a protodiatreme.

The composition of the dikes and the presence of mantle xenoliths support derivation of the dike magmas from the mantle, but no features of deposits or their contacts at the Black Canyon vent area indicate that eruptions were driven by the extremely high pressure of a deep-seated source. Instead, as noted above, we see evidence for a relatively few phreatomagmatic eruptions in the vent area. If the dikes were injected directly from mantle levels, some deficiency—either of magma volume or pressure, or both—limited intrusive and eruptive events. We conclude that the vent area formed from explosive interaction between intrusive magma and water-bearing sediments near the surface. The abundance of volatiles in the host rock may have localized or even initiated eruptive activity.

STRUCTURES AND INTRUSIVE PROCESS OF THE DIKE ARRAYS

North of the vent area, the localized magnetic expressions of the dikes indicate that they are not underlain by larger magmatic masses. No eruptive deposits crop out in association with the dike arrays, nor have we seen any deposits interbedded in fanglomerate. The marked relief of dike exposures in washes, gaps in outcrops of continuous dike segments on ridge tops, the common presence of fanglomerate wall-rock inclusions and of vertical joints related to an upper cooling surface suggest that the present erosional surface is close to the upper contacts of the dike segments.

The northeastern dike at Shiprock, New Mexico, studied in detail by Delaney and Pollard (1981), provides a good model for interpreting the outcrop pattern of Black Canyon dike segments. Deflection of dike tips between offset segments and bulbous swellings are observed at both localities. Delaney and Pollard (1981) showed that tip deflections are produced by mutually interfering stress fields localized around the intrusive tips. These stress fields interact because the dike segments were all intruded virtually simultaneously and do not each represent discrete, independent conduits connected to a magma source in the deep crust or upper mantle.

In the idealized dike depicted by Delaney and Pollard (1981; fig. 5), each segment is a sheetlike extension that merges downward into a main dike. The main dike grows by sending out these smaller extensions (or "fingers"—Baer and Reches, 1987) into the country rocks above or ahead of the main magma conduit. If the pressure and supply of magma are maintained, the magma extensions may coalesce by dilation of the country rocks, and this causes the conduit to grow laterally and upward (Delaney and Pollard, 1981). If the uppermost extensions never coalesce, the cooled dike consists of a main tabular sheet of crystallized magma with subordinate sheets projecting from many sites (fig. 5).

Like the bulbous swellings of the Black Canyon dikes, "buds" (Delaney and Pollard, 1981) at Shiprock are located at sites where brecciated country rock is seen in the dike. According to Delaney and Pollard (1981), the dike formed buds by abrasion erosion and brecciation of wall rocks during intrusion, a process that allowed the magma conduit to increase in width. Delaney and Pollard (1980) also suggested that plugs related to the northeastern Shiprock dike probably originated as bulbous swellings or buds, which enlarged enough to become volcanic vents. Buds also might be sites of dike branching (Delaney and Pollard, 1981).

Using the model of Delaney and Pollard (1981), the Black Canyon dikes probably constitute as few as three different intrusive sheets. Dike segments between locations 1 and 6 (fig. 1) are related to a main northeastern dike, segments between locations 7 and 11*B* are upper parts of a northwestern dike, and segments at locations 12 and 13 and south of Highway 93 are all extensions from the third dike.

Other than in the vent area discussed above, the Black Canyon dikes have no observable branches or vents, probably because all exposures are so close to the preerosional surface. Bulbous swellings clearly formed from the incorporation of easily eroded fanglomerate masses by dike magma (fig. 14). With only one exception, all internal chilled zones are adjacent to pods of incorporated fanglomerate. If bulbous swellings initiate plugs, which are eruptive vents, as concluded by Delaney and Pollard (1981), the evidence of that relation remains unexposed beneath the vent area. Although the magnetic anomaly over the vent area could be caused by a plug, we prefer to interpret the source of the anomaly as many smaller intrusions of variable magnetization, because this relation is observed in outcrops.

Our study found no definitive evidence of the likely sequence of intrusive and eruptive events. Campbell and Schenk (1950) suggested that the Black Canyon vent area formed after injection of the dike swarm, but the evidence does not preclude the possibility that intrusions and phreatic eruptions formed the vent area first, after which intrusion shifted to the north.

Measurement of directional indicators of dike propagation is limited by the degree of exposure (Delaney and Pollard, 1981). Features such as "cusps" (fig. 5; Delaney and Pollard, 1981), or grooves in wallrock at the dike contacts (Baer and Reches, 1987) may be used to determine propagation direction for a swarm. However, features such as cusps must be exposed below the level of the magmatic extensions to be reliable, and the wall rocks must be cohesive enough to preserve measurable striations. None of these requirements is fulfilled at Black Canyon.

If inclusion concentrations and the symmetrical arrangement of inclusion sizes in the Black Canyon dikes are due to flow sorting (see below), the longitudinal coalescence of disaggregated fanglomerate into the conduit axis of the dike segment at location 3 can be interpreted to support a south to north flow of magma in that dike segment. The limited value of this speculation is further constrained by the lack of exposure. Propagation directions may also be inferred from fanning of the dike system (Baer and Reches, 1987), but this inference is statistically based and requires a larger number of exposed dike segments and arrays than we can find in the Black Canyon area.

ORIGIN OF THE MAFIC-ULTRAMAFIC INCLUSION SUITE AND HOST MAGMA

Principal features that support a deep origin for mafic inclusions in the Black Canyon dikes include (1) the presence of kaersutite megacrysts in association with magnesian peridotite xenoliths, including kaersutite-bearing types; (2) intergrowths of kaersutite and aluminous clinopyroxene; (3) the overwhelming abundance of cleavage or irregular anhedral shapes among the kaersutite crystals; and (4) melting or fragmentation of kaersutite megacrysts in the host basalt. The absence of correlation between megacryst compositional variations and positions of the analyzed samples in the dike at location 13 shows further that crystallization differentiation did not occur in place.

The compositions of mafic megacrysts in the Black Canyon dikes, especially of kaersutite and associated pyroxene, are comparable with those reported for high-pressure megacryst suites worldwide (Wilshire and Trask, 1971; Best, 1974; Irving, 1974, 1977). The association of kaersutite and Fe-rich aluminous pyroxene with peridotite and Al-augite-bearing xenoliths in the Black Canyon dikes and tuff breccia is common at xenolith-megacryst localities elsewhere in the world (for example, Wilshire and Binns, 1961; Best, 1970, 1974; Irving, 1974; Wilkinson, 1975; Wilshire and Shervais, 1975; Wass, 1979; Wilshire and others, 1980). The presence of this association in the Black Canyon suite further supports the idea of a common origin for the mafic megacrysts and xenoliths (Wilshire and Trask, 1971; Best, 1974; 1975; Irving, 1980; Wilshire and others, 1988).

Kaersutite and kindred high-pressure mafic minerals in basaltic lavas may form either from crystallization in the host magma at high pressure ("high-pressure phenocrysts"—Binns, 1969; Green and Hibberson, 1970; Binns and others, 1970; Wilkinson, 1975; Wass, 1979) or may be accidental inclusions from the fragmentation of polycrystalline aggregates (dikes or veins) already present in the mantle (Best, 1970; Wilshire and Trask, 1971; Irving, 1974). The shapes, reaction textures, and compositions of the mafic megacrysts, as well as the isotopic disequilibrium between kaersutites and dike rock at the Black Canyon locality (Basu, 1978; Foland and others, 1980), indicate that these amphiboles are not cognate to the magma and thus are xenocrysts.

Clinopyroxene megacrysts are of low abundance in the inclusion suite compared to kaersutites, and the compositional variation between clinopyroxenes of the megacryst suite and poikilitic grains in wehrlitic xenoliths is not as well delineated. Because clinopyroxene megacrysts have compositions that overlap the poikilitic grains in peridotite, they could have a common origin. Therefore, clinopyroxene megacrysts might be either xenocrysts or high-pressure phenocrysts.

Campbell and Schenk (1950) classified the dikes as camptonite because they assumed that the large kaersutite grains crystallized in place. According to Sørenson (1974), camptonite is an intrusive alkali gabbro containing cognate sodic amphiboles, titanaugite, and biotite±olivine. However, the Black Canyon dikes do not fit these criteria because the amphiboles are neither sodic nor cognate. We prefer to classify the dikes by the compositions of matrix and the main matrix minerals, Ti-augite and olivine. These minerals, the norms of unleached rocks, and the isotopic composition of matrix samples are all characteristic of alkali olivine basalt. Therefore, alkali olivine basalt probably is the best petrologic designation for the dike rocks.

Mantle xenoliths of the inclusion suite, as well as the isotopic composition of the matrix (Basu, 1978; Foland and others, 1980) indicate a mantle origin for the Black Canyon alkali olivine basalt magma. Numerous studies (for example, Frey and Green, 1974; Hutchison and others, 1975; Wass and others, 1980; Boettcher and O'Neil, 1980) have shown that alkali basalts cannot be produced by the melting of anhydrous peridotites with compositions similar to the most common xenolith types in suites from either kimberlite or basalt. At least one precursory event must add the incompatible elements—such as Na, K, and Ti and minor elements such as U, Th, and LREE—to parental mantle

peridotite in order for it to produce basaltic magma from partial melting.

Geochemical studies of xenoliths show that magnesian mantle peridotites can become enriched in incompatible trace elements by metasomatism and remain relatively refractory in major-element composition (for example, Kempton, 1987; McDonough and Frey, 1989). Composite xenoliths of peridotite in contact with kaersutite- or biotite-rich rocks, Al-augite pyroxenite, and hybrids of these lithologic types have been shown to be mafic intrusions in peridotite (Wilshire and Shervais, 1975; Irving, 1980; Wilshire and others, 1980; Menzies and others, 1985; Nielson and others, 1993). These intrusions represent mantle magmas that locally metasomatized peridotite wall rock, enriching it in incompatible elements, before generation of the xenolith host basalt. Xenolith-megacryst suites, including composite xenoliths and megacrysts with compositions similar to those of minerals in mantle intrusions, are found (1) in Arizona at the north rim of the Grand Canyon (Best, 1974, 1975) and in the San Carlos and Four Corners areas (Wilshire and others, 1988), (2) in New Mexico at Kilbourne Hole (Wilshire, Schwarzman, and Trask, 1971; Irving, 1980; Roden and others, 1988), and (3) in California at Dish Hill, Deadman Lake (Wilshire and Trask, 1971; Wilshire and others, 1980; Nielson and others, 1993), and the Cima volcanic field (Wilshire and others, 1991).

Although the most abundant high-pressure inclusions in the Black Canyon dikes are amphibole xenocrysts and relatively minor peridotite xenoliths, the origin of megacrysts from a source within mantle peridotite is shown by (1) olivine-rich xenoliths that contain interstitial amphibole, (2) a composite sample with a thin kaersutite vein, and (3) reports of amphibole-bearing pyroxenites (A.J. Irving, written commun., 1983). Clinopyroxene compositions from Group I Black Canyon xenoliths have widely variable contents of incompatible elements, including the LREE (Roden and Shimizu, 1989). Such wide variations can occur in regions where LREE-enriched magma intruded and locally metasomatized refractory peridotite (Wass and others, 1980; Reisberg and Zindler, 1986; O'Reilly and Griffin, 1988; Nielson and others, 1993). The kaersutite xenocryst analyzed by Irving and Frey (1984) is relatively enriched in LREE and could represent a metasomatizing melt. Therefore, the mafic-ultramafic suite of inclusions in Black Canyon dikes could be derived from a mantle source analogous to ones rich in pyroxenite xenoliths, such as Lunar Crater, Nevada (Bergman and others, 1981).

We conclude that the physical and chemical evidence strongly suggests that the xenocryst-xenolith suite in Black Canyon dikes probably came from a region of peridotite that had been invaded locally by a large volume of hydrous alkali basalt magma. The magma crystallized to form a dense complex of kaersutite-rich pyroxenites and hornblendite dikes and veins (O'Reilly and Griffin, 1988; Griffin and others, 1988; Nielson and others, 1993). Similar to outcrops of hornblendite rock types in the peridotite massif at Lherz, France (Conquéré, 1970). Coarse-grained dikes probably were broken up by the later dike magma, thus producing the large kaersutite xenocrysts that are found in the Black Canyon dikes.

ORIGIN OF ZONING AND INCLUSION DISTRIBUTION PATTERNS

ZONING

Our observations of all the dikes in Black Canyon arrays show that the "zoning" described by Campbell and Schenk (1950) is a rare combination of features that are all present coincidentally in the dike segment at location 13 and are all oriented parallel or nearly parallel to the longitudinal contacts and axial planes of dikes. These features include alternating fissile and massive matrix-structure zones that change in position and symmetry along strike, elongation of tabular vesicles, and preferred orientation of tabular matrix grains and inclusions. Flow banding (fig. 10), chilled internal zones, and incorporated fanglomerate masses are the only notable internal features of the Black Canyon dikes that are not seen in the exposures at location 13. The dike segment at location 13 also contains abundant inclusions (including rare clasts from the fanglomerate) that are concentrated in the dike axial zone and are sorted symmetrically, by size, about the axis.

We believe that the alternations of matrix fissility and the alignments of tabular vesicles and xenocrysts are the preserved patterns of magma flow during intrusion. Platy or elongate rock fragments, bubbles, and crystals being carried in the magma were oriented within the longitudinal flow planes. The constant matrix grain size across the dike segment at location 13 suggests that all internal zones cooled at the same rate after the magma had stagnated. Shear planes present in the last stage of intrusion became flow banding or longitudinal joint planes as the rate of flow decreased and cooling began.

Three or more symmetrical, regularly alternating zones are rarely observed in the Black Canyon dikes; these zones probably represent stable laminar-flow regimes that persisted only locally within individual dike segments. Enlargement of the magma conduit by erosion of fanglomerate wall rock promoted development of turbulent-flow vortices. Bulbous swellings grew at the sites of erosion. When the vortices cooled, they were preserved as curved joint planes.

INCLUSION CONCENTRATIONS AND SIZE SORTING

Campbell and Schenk's (1950) hypothesis and other similar hypotheses about the origin of the supposed zoning in the dike segment at location 13 are all based on the

distribution and size sorting of inclusions. The interpretation of Campbell and Schenk (1950) that the kaersutites crystallized in place is clearly refuted by the compositional data summarized above. An alternative idea is that the zones at location 13 formed from multiple injections of magma into established dike conduits (F.J. Spera, written commun., 1984), but this hypothesis is not substantiated by the structural and textural relations we recorded in all other Black Canyon dike segments.

Black Canyon dike segments contain axial inclusion concentrations only where inclusions are abundant. Segments with relatively few inclusions show no particular distribution of particles or particle sizes with respect to structural zones. All exposed dike tips and most chilled margins are relatively barren of inclusions. The original dike crests are either eroded or unexposed, but they probably were wedge shaped, like dike tips. At location 13, kaersutite grains are the most numerous inclusions, but the three other segments with axial inclusion concentrations have populations in which fanglomerate clasts predominate. These relations, as well as Delaney and Pollard's (1981) study of the northeastern Shiprock dike, lead us to conclude that masses of fanglomerate country rocks were eroded by the intruding magma and incorporated into the Black Canyon dikes through the large surface area at the vertical dike/fanglomerate contact walls. To form axial concentrations, fanglomerate inclusions must have traversed the relatively barren dike margins after the masses became disaggregated.

Bulbous swellings formed at the sites of fanglomerate erosion and incorporation. The common presence of fanglomerate masses in tabular dike segments near bulbous swellings, such as at locations 2 and 11*A* (figs. 1, 6*A*, *B*), show that incorporated clasts may be swept from the enlarging magma conduit into an adjacent tabular dike segment. Regularly alternating matrix structure zones are observed in three tabular dike segments that contain a large volume of inclusions (tables 1, 2). Measurements at location 13 show that the smallest particle sizes are present in all zones internal to the dike contacts, whereas the size of the largest inclusions increases from the dike contacts to the axis, forming a log-normal distribution. This particle distribution implies a stable configuration of the flow regime in this dike segment. The regular alternation of fissility suggests further that the flow regime was laminar. We speculate that large volumes of inclusions may produce, or help stabilize, local laminar-flow regimes.

Size-sorted inclusion concentrations (the "zoning" described by Campbell and Schenk, 1950) also occur only in dike segments with abundant inclusions (table 2). At location 13, both near-surface fanglomerate clasts and kaersutite xenocrysts from the mantle were concentrated in the axial zones, and the largest inclusion sizes are found in the innermost axial zone. Therefore, whether or not the dikes represent multiple injections of magma, the process that concentrated and sorted the inclusions must be related to a mechanical process in the magma conduits and not to melting or extraction of magma in the mantle. We conclude that the characteristics of the axial concentrations and size sorting of inclusions in the Black Canyon dikes resemble flow-sorting phenomena.

Evidence for efficient flow-sorting processes in the Black Canyon dikes is seen at location 2 (figs. 1, 7*B*). The breccia at this locality probably formed when a mass of friable fanglomerate was incorporated into the contact zone at a level not far below the modern surface. At the present level of exposure, this partly disaggregated mass of wall rock, including clasts, sandy matrix, and chilled fragments of dike matrix, lies between the contact and dike axial zones. These clasts must have migrated from the contact zone toward the dike axis as they were carried both laterally and upward by the flowing magma. At location 3, fragments of partly disaggregated fanglomerate are found in the dike margin, but a short distance to the north they are concentrated into the dike axial zone. This south to north change from marginal incorporation to axial inclusion concentration may show that the magma in this dike segment was moving northward.

Flow sorting (Drever and Johnston, 1958), both of phenocrysts in magmatic bodies and of exotic fragments in brecciated intrusive bodies, is a widely reported phenomenon. For example, Baragar (1960) noted that axial concentrations of the largest fragment sizes characterize fibers of wood pulp in slurries. A similar phenomenon, sorting of noncognate fragments in intrusions, was reported by Reynolds (1954) for subvolcanic breccia at several Irish localities; by Wilshire (1961) for sedimentary fragments in a dike near Sydney, Australia; and by Wilshire, Offield, and Howard (1971) for coarse particles in nonfluid intrusive impact breccia at the Sierra Madera structure, Texas. Quasiscale-model experiments by Bhattacharji and Smith (1964) and Bhattacharji (1967) demonstrated that particles are sorted toward the axial parts of a conduit by flowing magmalike fluids.

Concentrations of olivine in the centers of basaltic dikes and slightly below the central zones of sills were ascribed to flow sorting by Bowen (1928, p. 145), Drever and Johnston (1958, 1967), Baragar (1960), Simkin (1967), and Gibb (1968). Bébièn and Gagny (1979) reported that all phenocryst species (olivine+pyroxene+plagioclase) and even early formed matrix minerals are sorted into the central zones of dikes at a Greek ophiolite complex. These examples show that sorting is a common process in flowing magmas. However, current models for phenocryst concentration tend to favor accretionary crystallization, rather than flow sorting or flow differentiation, because accretion models allow the dike to be interpreted as a time profile (Platten and Watterson, 1987).

Komar (1972, 1976) attributed the inward migration of particles in natural conduits to grain-dispersive pressures.

He also demonstrated that such pressures are larger than those related either to velocity gradients in the host fluid, to wall effects, or Magnus-type forces. Grain-dispersive pressure is due to grain-fluid or grain-grain interactions, depending on the parameters of the system. These pressures become important when a fluid contains more than 8 percent particles (Komar, 1972). The effect of dispersive pressures may also depend upon particle size. These characteristics fit our observation that axial inclusion concentrations and size sorting are only seen where inclusions are abundant (greater than 10 percent) and where axial and near axial concentrations contain inclusion sizes of at least 20 mm (table 2).

Axial concentrations of mantle xenocrysts may be produced by sorting pressure anywhere between the mantle source region and the present erosional surface, but the concentrations of fanglomerate inclusions in Black Canyon dikes must form between the depositional base of the fanglomerate and the surface. This distance is unknown for the Black Canyon area, but the fanglomerate unit is as much as several hundred meters thick elsewhere (I. Lucchitta, oral commun., 1992). Therefore, long distances of vertical flow are not required to produce size sorting of abundant inclusions with an appropriate range of grain size.

Delaney and Pollard's (1981) model of dike growth implies that the sorting in Black Canyon dikes may take place over an even shorter vertical distance, depending upon the level at which individual dike segments formed as offshoots from the main dike. If the segments connect with the main dike above the base of fanglomerate deposits, this would imply that sorting processes are extremely efficient.

SUMMARY

The Black Canyon dikes are alkali olivine basalt intrusions and related ejecta; the content of mafic and ultramafic inclusions indicates derivation of the dike magma from the mantle. Substantial textural and isotopic disequilibrium between the host dike matrix and kaersutite megacrysts shows that the amphiboles could not have crystallized from the host magma, either in the crust or upper mantle, and thus are xenocrysts.

Identification of the kaersutite+clinopyroxene inclusions as xenocrysts requires reinterpreting the petrologic classification and petrogenesis of the Black Canyon dikes. Kaersutite grains that accompany orthopyroxene in a vein in a lherzolite xenolith have compositions identical to the bulk of the xenocrysts, and amphiboles with variable magnesian compositions are found as interstitial grains in altered wehrlitic xenoliths. Thus, the mafic-ultramafic inclusion suite may represent a mantle region of peridotite that was intruded and metasomatized by hydrous basaltic magmas some time before the generation of melts that formed the Black Canyon dikes. The mafic megacrysts were coarse veins and dikes that crystallized in this older magmatic episode. Most feldspathic and silicic minerals and lithic inclusions in the dikes apparently come from fanglomerate host rocks of the dike swarm, although anorthoclase and some plagioclase grains probably derive from deep crustal levels.

Zoning in the Black Canyon dikes is commonly defined by irregular and, less commonly, regular alternations of massive and fissile matrix structure that resemble flow patterns in streams. These zones are joint patterns inherited from shear planes and boundaries between magmatic flow regimes in the dike conduits. The joints and other features related to flow generally are parallel to the axial plane of the dike and may occur individually or in combination. The more regular symmetrical or asymmetrical textural zones are rare, and they probably represent local stable-flow regimes that formed and persisted over very short distances.

The rare axial concentration and size sorting of inclusions affects both mantle- and near-surface-derived inclusions from Miocene and Pliocene fanglomerate wall rocks in the best exposed dike (location 13; fig. 1) and other Black Canyon dikes. The log-normal distribution of the largest inclusion sizes in the dike segment at location 13 indicates that mantle- and crustal-derived fragments were carried in a stable laminar-flow regime. Most inclusion concentration filaments are parallel to other flow-generated structures; the filaments are present only where inclusions are abundant and where maximum particle sizes reach 20 mm or greater and, except at location 13, the most common inclusions are fanglomerate clasts. Thus, the most likely origin for the size distributions and concentration of inclusions is from flow sorting of particles in magma in the dike conduit and is unrelated to deep-seated magmatic processes or repeated injections of magma into near-surface conduits.

REFERENCES CITED

Alibert, Chantal, Michard, Annie, and Albarède, Francis, 1986, Isotope and trace element geochemistry of Colorado Plateau volcanics: Geochimica et Cosmochimica Acta, v. 50, p. 2735-2750.

Anderson, R.E., 1971, Thin skin distension in Tertiary rocks of southeastern Nevada: Geological Society of America Bulletin, v. 82, p. 43-58.

———1978, Geologic map of the Black Canyon quadrangle, Mohave County, Arizona, and Clark County, Nevada: U.S. Geological Survey Map, GQ 1394, scale 1:62,500.

Anderson, R.E., Longwell, C.E., Armstrong, R.L., and Marvin R.F., 1972, Significance of K-Ar ages of Tertiary rocks from the Lake Mead region, Nevada-Arizona: Geological Society of America Bulletin, v. 83, p. 273-288.

Baer, Gideon, and Reches, Ze'ev, 1987, Flow patterns of magma in dikes, Makhtesh Ramon, Israel: Geology, v. 15, p. 569-572.

Baragar, W.R.A., 1960, Petrology of basaltic rocks in part of the Labrador trough: Geological Society of America Bulletin, v. 71, p. 1589-1644.

Basu, A.R., 1978, Trace elements in mantle-derived minerals: Geochimica et Cosmochimica Acta, v. 42, p. 659-668.

Bébièn, J., and Gagny, C.l., 1979, Importance of flowage differentiation in magmatic evolution; an example from an ophiolitic sheeted complex: Journal of Geology v. 87, p. 579-582.

Bergman, S.C., Foland, K.A., and Spera, F.J., 1981, On the origin of an amphibole-rich vein in a peridotite inclusion from the Lunar Crater volcanic field, Nevada, U.S.A.: Earth and Planetary Science Letters, v. 56, p. 343-361.

Best, M.G., 1970, Kaersutite-peridotite inclusions and kindred megacrysts in basanitic lavas, Grand Canyon, Arizona: Contributions to Mineralogy and Petrology, v. 27, p. 25-44.

———1974, Mantle-derived amphibole within inclusions in alkalic-basaltic lavas: Journal of Geophysical Research, v. 79, p. 2107-2113.

———1975, Amphibole-bearing cumulate inclusions, Grand Canyon, Arizona and their bearing on silica-undersaturated magmas in the upper mantle: Journal of Petrology, v. 16, p. 212-236.

Bhattacharji, Somdev, 1967, Mechanics of flow differentiation in ultramafic and mafic sills: Journal of Geology v. 75, p. 101-112.

Bhattacharji, Somdev, and Smith, C.H., 1964, Flowage differentiation: Science, v. 145, p. 150-152.

Binns, R.A., 1969, High-pressure megacrysts in basanitic lavas near Armidale, New South Wales: American Journal of Science, Schairer Volume, v. 267-A, p. 33-49.

Binns, R.A., Duggan, M.B., Wilkinson, J.F.G., and Kalocsai, G.I., 1970, High pressure megacrysts in alkaline lavas from northeastern New South Wales: American Journal of Science, v. 269, p. 132-168.

Boettcher, A.L., and O'Neil, J.R., 1980, Stable isotope, chemical, and petrographic studies of high-pressure amphiboles and micas; evidence for metasomatism in the mantle source regions of alkali basalts and kimberlites: American Journal of Science, Jackson Volume, v. 280-A, p. 594-621.

Bowen, N.L., 1928, The evolution of the igneous rocks: New Jersey, Princeton University Press, 334 p.

Cameron, Maryellen, and Papike, J.J., 1981, Structural and chemical variations in pyroxenes: American Mineralogist, v. 66, p. 1-50.

Campbell, Ian, and Schenk, E.T., 1950, Camptonite dikes near Boulder Dam, Arizona: American Mineralogist, v. 35, p. 671-692.

Conquéré, Ferdinand, 1970, La lherzolite à amphibole du gisement de Caussou, Ariège, France: Contributions to Mineralogy and Petrology, v. 30, p. 296-313.

Daley, E.E., and DePaolo, D.J., 1992, Isotopic evidence for lithospheric thinning during extension; southeastern Great Basin: Geology, v. 20, p. 104-108.

Dawson, J.B., 1967, A review of the geology of kimberlite, *in* Wyllie, P.J., ed., Ultramafic and related rocks: New York, John Wiley and Sons, p. 241-251.

Delaney, P.T., and Pollard, D.D., 1981, Deformation of host rocks and flow of magma during growth of minette dikes and breccia-bearing intrusions near Shiprock, New Mexico: U.S. Geological Survey Professional Paper 1202, 61 p.

Drever, H.L. and Johnston, R., 1958, The petrology of picritic rocks in minor intrusions—a Hebridean group: Royal Society of Edinburgh Transactions, v. 63, p. 459-499.

———1967, Picritic minor intrusions, in Wyllie, P.J., ed., Ultramafic and Related Rocks: New York, John Wiley, p. 71-82.

Faulds, J.E., Geissman, J.W. and Mawer, C.K., 1990, Structural development of a major extensional accommodation zone in the Basin and Range province, northwestern Arizona and southern Nevada; implications for kinematic models of continental extension, *in* Wernicke, B.W., ed., Basin and Range extensional tectonics near the latitude of Las Vegas, Nevada: Geological Society of America Memoir 176, p. 37-76.

Fodor, R.V., 1978, Ultramafic and mafic inclusions and megacrysts in Pliocene basalt, Black Range, New Mexico: Geological Society of America Bulletin, v. 89, p. 451-459.

Foland, K.A., Spera, F.J., and Bergman, S.C., 1980, Strontium isotope relations in megacryst-bearing camptonites from NW Arizona [abs.]: Geological Society of America Abstracts with Programs, v. 12, p. 36.

Frey, F.A., and Green, D.H., 1974, The mineralogy, geochemistry and origin of lherzolite inclusions in Victorian basanites: Geochimica et Cosmochimica Acta, v. 38, p. 1023-1059.

Garcia, M.O., Muenow, D.W., and Liu, N.W.K., 1980, Volatiles in Ti-rich amphibole megacrysts, southwest USA: American Mineralogist, v. 65, p. 306-312.

Gibb, F.G.F., 1968, Flow differentiation in the xenolithic ultrabasic dikes of the Cuillins and the Strathaird Peninsula, Isle of Skye, Scotland: Journal of Petrology, v. 9, p. 411-443.

Green, D.H., and Hibberson, W., 1970, Experimental duplication of conditions of precipitation of high pressure phenocrysts in a basaltic magma: Physics of the Earth and Planetary Interiors, v. 3, p. 247-254.

Griffin W. L., O'Reilly S. Y., and Stabel A., 1988, Mantle metasomatism beneath western Victoria, Australia II; isotopic geochemistry of Cr-diopside lherzolites and Al-augite pyroxenites: Geochimica et Cosmochimica Acta, v. 52, p. 449-460.

Howard, K.A., and John, B.E., 1987, Crustal extension along a rooted system of imbricate low-angle faults; Colorado River extensional corridor, California and Arizona, *in* Coward, M.P., Dewey, J.F., and Hancock, P.L., eds., Continental extensional tectonics: London, Geological Society Special Publication 28, p. 299-311.

Hutchison, R., Chambers, A.L., Paul, D.K., and Harris, P.G., 1975, Chemical variation among French ultramafic xenoliths—Evidence for a heterogeneous upper mantle: Mineralogical Magazine, v. 40, p. 153-170.

Irving, A.J., 1974, Megacrysts from the Newer Basalts and other basaltic rocks of southeastern Australia: Geological Society of America Bulletin, v. 85, p. 1503-1514.

———1977, Origin of megacryst suites in basaltic dikes near 96 Ranch, west Texas and Hoover Dam, Arizona [abs.]: Eos, Transactions of the American Geophysical Union, v. 58, p. 526.

———1980, Petrology and geochemistry of composite ultramafic xenoliths in alkalic basalts and implications for magmatic processes within the mantle: American Journal of Science, Jackson Volume, v. 280-A, p. 389-427.

Irving, A.J., and Frey, F.A., 1984, Trace-element abundances in megacrysts and their host basalts; constraints on partition coefficients and megacryst genesis: Geochimica et Cosmochimica Acta, v. 48, p. 1201-1221.

Kempton, P.D., 1987, Mineralogic and geochemical evidence for differing styles of metasomatism in spinel lherzolite xenoliths; enriched mantle source regions of basalts?, *in* Menzies, M.A. and Hawkesworth, C.J., eds., Mantle metasomatism: New York, Academic Press, p. 45-89.

Komar, P.D., 1972, Mechanical interactions of phenocrysts and flow differentiation of igneous dikes and sills: Geological Society of America Bulletin, v. 83, p. 973-988.

———1976, Phenocryst interactions and the velocity profile of magma flowing through dikes or sills: Geological Society of America Bulletin, v. 87, p. 1336-1342.

Leake, B.E., 1978, Nomenclature of amphiboles: American Mineralogist, v. 63, p. 1023-1052.

McDonough W. F., and Frey, F.A., 1989, Rare earth elements in upper mantle rocks, *in* Ribbe, P.H., ed., Geochemistry and mineralogy of rare earth elements: Mineralogical Society of America, Reviews in Mineralogy, v. 21, p. 99-145.

Menzies, M.A., Kempton, P.D., and Dungan, Michael, 1985, Interaction of continental lithosphere and asthenospheric melts below the Geronimo volcanic field, Arizona, U.S.A.: Journal of Petrology, v. 26, p. 663-693.

Mukasa, S.B., Shervais, J.W., Wilshire, H.G., and Nielson, J.E., 1991, Intrinsic Nd, Pb and Sr isotopic heterogeneities exhibited by the Lherz alpine peridotite massif, French Pyrenees: Journal of Petrology, Special Lherzolites Issue, p. 117-134.

Nielson, J.E., Budahn, J.R., Unruh, D.M., and Wilshire, H.G., 1993, Actualistic models of mantle metasomatism documented in a composite xenolith from Dish Hill, California: Geochimica et Cosmochimica Acta, v. 57, p. 105-121.

O'Reilly S. Y., and Griffin W. L., 1988, Mantle metasomatism beneath western Victoria, Australia I; metasomatic processes in Cr-diopside lherzolites: Geochimica et Cosmochimica Acta, v. 52, p. 433-449.

Papike, J.J., Ross, Malcolm, and Clark, J.R., 1969, Crystal-chemical characterization of clinoamphiboles based on five new structure refinements: Mineralogical Society of America Special Paper 2, p. 117-136.

Platten, I.M., and Watterson, J., 1987, Magma flow and crystallization in dyke fissures, *in* Halls, H.C., and Fahrig, W.F., Mafic dyke swarms: Geological Society of Canada Special Paper 34, p. 65-73.

Reisberg, Laurie, and Zindler, Allen, 1986, Extreme isotopic variations in the upper mantle; evidence from Ronda: Earth and Planetary Science Letters, v. 81, p. 29-45.

Reynolds, D.L., 1954, Fluidization as a geological process, and its bearing on the problem of intrusive granites: American Journal of Science, v. 252, p. 577-614.

Roden, M.F., Irving, A.J., and Murthy, V.R., 1988, Isotopic and trace element composition of the upper mantle beneath a young continental rift; results from Kilbourne Hole, New Mexico: Geochimica et Cosmochimica Acta, v. 52, p. 461-474.

Roden, M.F., and Shimizu, N., 1989, Compositional differences in the upper mantle between the Colorado Plateau and the Basin and Range provinces [abs.]: Eos, Transactions of the American Geophysical Union, v. 70, p. 509.

Ross, C.S., Foster, M.D., and Myers, A.T., 1954, Origin of dunites and of olivine-rich inclusions in basaltic rocks: American Mineralogist, v. 39, p. 693-737.

Simkin, Thomas, 1967, Flow differentiation in the picritic sills of North Skye, *in* Wyllie, P.J., ed., Ultramafic and related rocks: New York, John Wiley and Sons, p. 64-68.

Sørenson, H., 1974, Glossary of alkaline and related rocks (Appendix 2), *in* Sørenson, H., ed., The alkaline rocks: New York, John Wiley and Sons, p. 558-577.

Spray, J.G., 1982, Mafic segregations in ophiolite mantle sequences: Nature, v. 299, p. 524-528.

Wass, S.Y., 1979, Multiple origins of clinopyroxenes in alkali basaltic rocks: Lithos, v. 12, p. 115-132.

Wass, S.Y., Henderson, Paul, and Elliot, C.J., 1980, Chemical heterogeneity and metasomatism in the upper mantle; evidence from rare earth and other elements in apatite-rich xenoliths in basaltic rocks from eastern Australia: Philosophical Transactions of the Royal Society of London, v. A297, p. 333-346.

Wilkinson, J.F.G., 1975, Ultramafic inclusions and high pressure megacrysts from a nephelinite sill, Nandewar Mountains, northeastern New South Wales, and their bearing on the origin of certain ultramafic inclusions in alkaline volcanic rocks: Contributions to Mineralogy and Petrology, v. 51, p. 235-262.

Wilshire, H.G., 1961, Layered diatremes near Sydney, New South Wales: Journal of Geology, v. 69, p. 473-484.

Wilshire, H.G., and Binns, R.A., 1961, Basic and ultrabasic xenoliths from volcanic rocks of New South Wales: Journal of Petrology, v. 2, p. 185-208.

Wilshire, H.G., McGuire, A.V., Noller, J.S., and Turrin, B.D., 1991, Petrology of lower crustal and upper mantle xenoliths from the Cima volcanic field, California: Journal of Petrology, v. 32, p. 169-200.

Wilshire, H.G., Meyer, C.E., Nakata, J.K., Calk, L.C., Shervais, J.W., Nielson, J.E. and Schwarzman, E.C., 1988, Mafic and ultramafic xenoliths from volcanic rocks of the western United States: U.S. Geological Survey Professional Paper 1443, 179 p.

Wilshire, H.G., Offield, T.W., and Howard, K.A., 1971, Impact breccias in carbonate rocks, Sierra Madera, Texas: Geological Society of America Bulletin, v. 82, p. 1009-1018.

Wilshire, H.G., Pike, J.E.N., Meyer, C.E., and Schwarzman, E.C., 1980, Amphibole-rich veins in lherzolite xenoliths, Dish Hill and Deadman Lake, California: American Journal of Science, Jackson Volume, v. 280-A, p. 576-593.

Wilshire, H.G., Schwarzman, E.C., and Trask, N.J., 1971, Distribution of ultramafic xenoliths at 12 North American sites: NASA Interagency Report Astrogeology v. 42, p. 53-57.

Wilshire, H.G., and Shervais, J.W., 1975, Al-augite and Cr-diopside ultramafic xenoliths in basaltic rocks from western United States: Physics and Chemistry of the Earth, v. 9, p. 257-272.

Wilshire, H.G., and Trask, N.J., 1971, Structural and textural relationships of amphibole and phlogopite in peridotite inclusions, Dish Hill, California: American Mineralogist, v. 56, p. 240-255.

Table 4. Compositions of clinopyroxene.

[Analyses by electron microprobe, J.E. Nielson, U.S. Geological Survey, analyst. Determined on ARL model SEMQ, with 3 scanning and 6 fixed spectrometers; 15 kV accelerating voltage; sample currents 15-20 nA; count times 50-100 s. On-peak backgrounds; analyses monitored by internal standards. All grains examined for homogeneity; each analysis represents at least 5 analyzed spots per grain; L1-CAv, L7-CAv, and L4-CAv are average compositions of several grains. Data reduced using modified Bence-Albee corrections]

	Matrix clinopyroxene (MC)			Clinopyroxene megacrysts (CM)										
Sample No.	Z4-MC1	Z4-MC2	Z4-MC4	Y1-CM1	Y1-CM2	Y2-CM1	Y3-CM1	Y3-CM2	Y3-CM3	Y5-CM1	Y5-CM2	Y5-CM3	Z1-CM1	Z2-CM1
Analyses (weight percent oxide)														
SiO_2	47.2	43.8	48.6	48.1	48.0	48.8	49.6	49.8	48.0	49.2	49.6	49.6	49.0	48.6
Al_2O_3	5.7	9.5	4.7	7.7	7.7	7.7	7.2	7.2	8.0	7.3	7.1	7.0	7.8	7.9
FeO^{tot} [2]	7.1	7.8	7.3	6.6	6.6	6.6	5.8	5.8	6.8	5.8	5.7	5.8	6.4	6.6
MgO	12.5	10.9	12.9	14.1	13.7	13.9	14.0	13.8	13.6	13.8	13.9	13.9	13.8	13.7
CaO	22.1	23.1	23.1	20.6	20.5	20.2	19.5	19.4	21.0	19.8	19.6	19.5	20.4	20.4
Na_2O	0.46	0.68	0.46	1.2	1.2	1.2	1.1	1.1	1.2	1.1	1.1	1.1	1.2	1.2
TiO_2	3.4	4.7	3.4	1.7	1.8	1.7	1.7	1.7	2.0	1.8	1.7	1.7	1.8	2.0
MnO [3]	0.16	0.14	0.15	n.d.	n.d.	n.d.	0.13	0.13	n.d.	0.13	0.13	0.13	0.14	0.16
Cr_2O_3	0.06	0.02	0.02	0.57	0.41	0.51	0.32	0.35	0.41	0.31	0.35	0.36	0.35	0.30
Total	99.68	100.64	100.63	100.61	99.95	100.65	99.35	99.28	100.93	99.24	99.18	99.09	100.89	100.86
Mg ratio= Mg/(Mg+SFe)	.76	.71	.76	.79	.79	.79	.81	.81	.78	.81	.81	.81	.79	.79
Pyroxene structural formula														
Si	1.78	1.63	1.80	1.75	1.76	1.78	1.83	1.84	1.74	1.82	1.83	1.84	1.78	1.77
Al^{IV}	0.22	0.37	0.20	0.25	0.24	0.22	0.17	0.16	0.26	0.18	0.17	0.16	0.22	0.23
Al^{VI}	0.039	0.046	0.009	0.082	0.095	0.109	0.142	0.150	0.086	0.135	0.142	0.140	0.115	0.108
Fe^{II}	0.210	0.233	0.061	0.190	0.190	0.192	0.179	0.179	0.196	0.164	0.176	0.179	0.185	0.191
Mg	0.704	0.604	0.713	0.765	0.749	0.755	0.769	0.759	0.736	0.760	0.765	0.766	0.748	0.743
Mn	0.005	0.004	0.005	n.d.	n.d.	n.d.	0.004	0.004	n.d.	0.004	0.004	0.004	0.004	0.005
Ti	0.097	0.132	0.095	0.047	0.050	0.047	0.047	0.047	0.055	0.050	0.047	0.047	0.049	0.055
Cr	0.002	0.001	0.001	0.016	0.012	0.015	0.009	0.010	0.015	0.009	0.010	0.011	0.010	0.009
Ca	0.895	0.921	0.918	0.804	0.806	0.789	0.770	0.767	0.817	0.784	0.776	0.773	0.795	0.795
Na	0.034	0.049	0.033	0.085	0.085	0.085	0.079	0.079	0.085	0.079	0.079	0.079	0.085	0.085
En	38.94	36.44	39.04	46.98	45.68	45.60	44.87	44.51	45.19	44.54	44.56	44.59	45.12	45.06
Fs	11.56	8.04	10.70	3.66	5.18	6.75	10.20	10.50	4.64	9.52	10.26	10.44	6.92	6.71
Wo	49.50	55.52	50.26	49.35	49.14	47.65	44.93	44.99	50.17	45.94	45.18	44.97	47.95	48.24
CaTs [4]	21.55	18.95	19.69	28.65	27.40	25.99	20.25	20.71	28.64	21.13	19.94	19.79	25.43	26.13
Papike A/R [5]	A	A	A	A	A	A	A	R	A	A	A	R	A	A

Table 4. Compositions of clinopyroxene—Continued.

Sample No.	Clinopyroxenes in lherzolite xenoliths (L-C)																
	L1-C1	L1-C4	L1-CA[6]	L3-C2	L3-C4	L7-C1	L7-C3	L7-C6	L7-CA[6]	L4-C1	L4-C2	L4-C3	L4-C4	L4-C5	L4-C6	L4-C7	L4-CA[6]
Analyses (weight percent oxide)																	
SiO_2	51.2	51.2	51.3	50.9	51.4	52.1	52.2	52.3	52.3	51.4	50.6	50.7	51.0	51.3	51.5	51.3	51.6
Al_2O_3	5.9	5.9	6.0	6.1	5.9	5.4	5.4	5.5	5.4	4.3	4.4	4.4	4.4	4.4	4.4	4.3	4.4
FeO^{tot} [2]	3.2	3.3	3.2	3.2	3.2	3.3	3.2	3.3	3.3	4.7	4.6	4.7	4.7	4.7	4.7	4.6	4.7
MgO	16.1	16.0	16.0	15.9	16.1	16.6	16.2	16.2	16.2	15.4	15.6	15.6	15.4	15.5	15.2	15.3	15.2
CaO	19.7	19.9	19.9	19.7	19.7	19.9	19.9	20.0	19.9	22.2	22.3	22.4	22.5	22.5	22.4	22.4	22.1
Na_2O	1.0	1.0	1.0	1.0	0.97	0.92	0.92	0.93	0.92	0.66	0.64	0.63	0.64	0.64	0.66	0.65	0.64
TiO_2	0.32	0.32	0.33	0.59	0.57	0.32	0.31	0.32	0.32	0.69	0.63	0.65	0.64	0.69	0.71	0.69	0.70
MnO	0.10	0.10	0.10	0.09	0.09	0.10	0.10	0.10	0.10	0.11	0.10	0.10	0.10	0.11	0.10	0.11	0.11
Cr_2O_3	0.96	0.93	1.00	1.00	0.99	1.1	1.1	1.1	1.1	0.46	0.50	0.47	0.48	0.49	0.46	0.47	0.46
Total	98.48	98.65	98.83	98.48	98.92	99.74	99.33	99.75	99.54	99.92	99.37	99.65	99.86	100.33	100.13	99.82	99.91
Mg ratio= Mg/(Mg+SFe)	.90	.90	.90	.90	.90	.90	.90	.90	.90	.85	.86	.85	.85	.85	.85	.86	.85
Pyroxene structural formula																	
Si	1.88	1.88	1.88	1.87	1.88	1.89	1.90	1.90	1.90	1.88	1.86	1.86	1.86	1.87	1.88	1.88	1.89
Al^{IV}	0.12	0.12	0.12	0.13	0.12	0.11	0.10	0.10	0.10	0.12	0.14	0.14	0.14	0.13	0.12	0.12	0.11
Al^{VI}	0.135	0.133	0.137	0.135	0.134	0.121	0.132	0.132	0.132	0.065	0.048	0.046	0.055	0.057	0.070	0.064	0.079
Fe^{II}	0.097	0.095	0.098	0.098	0.098	0.100	0.097	0.100	0.100	0.138	0.132	0.134	0.136	0.136	0.140	0.136	0.141
Mg	0.881	0.874	0.873	0.871	0.878	0.897	0.879	0.876	0.877	0.839	0.853	0.851	0.839	0.841	0.827	0.835	0.829
Mn	0.003	0.003	0.003	0.003	0.003	0.003	0.003	0.003	0.003	0.003	0.003	0.003	0.003	0.003	0.003	0.003	0.003
Ti	0.009	0.009	0.009	0.016	0.016	0.009	0.008	0.009	0.009	0.019	0.017	0.018	0.018	0.019	0.019	0.019	0.019
Cr	0.028	0.027	0.029	0.029	0.029	0.032	0.032	0.032	0.032	0.013	0.015	0.014	0.014	0.014	0.013	0.014	0.013
Ca	0.775	0.782	0.780	0.776	0.772	0.774	0.776	0.777	0.775	0.870	0.877	0.879	0.882	0.878	0.876	0.879	0.867
Na	0.071	0.071	0.071	0.071	0.069	0.065	0.065	0.065	0.065	0.047	0.046	0.045	0.045	0.045	0.047	0.046	0.045
En	50.54	50.22	50.11	50.00	50.22	50.81	50.15	49.95	50.06	46.59	47.93	47.78	46.92	46.91	45.87	46.34	45.72
Fs	5.00	4.87	5.08	5.45	5.60	5.39	5.56	5.71	5.72	5.13	2.81	2.90	3.79	4.13	5.54	4.88	6.49
Wo	44.46	44.91	44.81	44.54	44.18	43.79	44.29	44.34	44.21	48.28	49.26	49.32	49.29	48.96	48.60	48.78	47.79
CaTs[4]	18.27	18.48	18.41	18.40	17.85	16.60	17.19	17.23	17.19	14.84	17.08	17.03	16.25	14.65	14.65	14.91	13.73
Papike A/R[5]	A	A	A	A	R	A	R	R	R	A	A	A	A	A	A	A	A

Table 4. Compositions of clinopyroxene—Continued.

Sample No.	Clinopyroxenes poikilitically intergrown with kaersutite in wehrlitic xenoliths (D-C)									
	D1-C1	D1-C2	D1-C3	D1-C3	D4-C3	D4-C2	D4-C3	D6-C1	D6-C2	D6-C3
Analyses (weight percent oxide)										
SiO_2	51.8	51.7	51.9	51.8	48.9	48.8	48.8	47.6	48.0	48.1
Al_2O_3	4.6	4.6	4.7	4.5	7.5	7.4	7.3	8.1	8.1	8.0
FeO^{tot} [2]	4.3	4.2	4.4	4.5	6.1	5.9	5.9	6.3	6.3	6.3
MgO	15.2	14.8	14.8	14.4	13.3	13.5	13.4	12.8	12.8	12.9
CaO	22.3	22.4	22.2	22.1	19.7	19.4	19.3	19.8	20.0	19.9
Na_2O	0.65	0.78	0.73	0.82	1.1	1.1	1.1	1.1	1.1	1.1
TiO_2	0.74	0.72	0.71	0.71	1.8	1.6	1.6	2.0	2.0	2.0
MnO	0.14	0.13	0.14	0.14	0.15	0.15	0.15	0.15	0.16	0.15
Cr_2O_3	0.13	0.13	0.13	0.13	0.30	0.52	0.51	0.20	0.21	0.20
Total	99.86	99.46	99.71	99.10	98.85	98.37	98.06	98.05	98.67	98.65
Mg ratio= Mg/(Mg+SFe)	.86	.86	.86	.85	.79	.80	.80	.78	.78	.78
Pyroxene structural formula										
Si	1.89	1.90	1.90	1.91	1.82	1.82	1.83	1.79	1.79	1.79
Al^{IV}	0.11	0.10	0.10	0.09	0.18	0.18	0.17	0.21	0.21	0.21
Al^{VI}	0.092	0.097	0.105	0.107	0.146	0.146	0.149	0.144	0.146	0.145
Fe^{II}	0.130	0.127	0.134	0.139	0.188	0.183	0.185	0.195	0.194	0.195
Mg	0.828	0.810	0.808	0.792	0.737	0.750	0.747	0.716	0.711	0.717
Mn	0.004	0.004	0.004	0.004	0.005	0.005	0.005	0.005	0.005	0.005
Ti	0.020	0.020	0.020	0.020	0.050	0.045	0.045	0.056	0.056	0.056
Cr	0.004	0.004	0.004	0.004	0.009	0.015	0.015	0.006	0.006	0.006
Ca	0.874	0.881	0.872	0.874	0.785	0.775	0.774	0.796	0.799	0.795
Na	0.046	0.056	0.052	0.059	0.079	0.080	0.080	0.080	0.080	0.080
En	45.56	44.92	44.57	43.88	43.22	44.11	43.81	42.67	42.29	42.52
Fs	6.38	6.21	7.36	7.70	10.75	10.31	10.82	9.88	10.19	10.31
Wo	48.06	48.88	48.07	48.42	46.03	45.58	45.37	47.45	47.51	47.16
CaTs [4]	13.18	13.77	13.01	13.07	21.15	21.44	20.89	23.80	23.34	22.98
Papike A/R [5]	A	A	A	R	A	A	A	A	A	A

[1] Sample numbers are for the dike segment at location 13: letter in prefix designates exposure Y or Z; prefix number refers to structural zone 1-5 (see table 2).
[2] Total Fe expressed as FeO.
[3] N.d., Mn not determined.
[4] Content of calcium-Tschermak's molecule.
[5] Analysis accepted (A) or rejected (R) by Cameron and Papike (1981) criteria. All "R" analyses listed were rejected on the basis of one criterion and are indistinguishable from "A" analyses.
[6] Average of several analyzed grains.

Table 5. Compositions of orthopyroxene.

Sample No.	Orthopyroxene in lherzolite (L-O)										Orthopyroxene in kaersutite vein (BC-2-21)		
	L1-O1	L1-O2	L1-O3	L1-O4	L5-O1	L5-O2	L5-O3	L5-O4	L5-O5	L6-O5	O1	O2	O3
Analyses (weight percent oxide)													
SiO_2	54.3	54.3	54.5	53.9	55.0	55.0	54.9	54.2	55.0	54.8	54.1	54.2	53.9
Al_2O_3	5.0	4.9	5.0	4.9	3.6	3.6	3.6	4.3	3.6	3.2	5.2	5.2	5.2
FeO^{tot} [1]	6.2	6.3	6.3	6.3	5.8	5.8	5.7	5.8	5.8	6.2	7.0	7.0	7.0
MgO	32.6	32.5	32.5	32.4	33.5	33.6	33.4	33.0	33.2	33.1	32.2	31.8	31.6
CaO	1.3	1.3	1.3	1.3	1.3	1.3	1.3	1.2	1.3	1.2	1.2	1.2	1.2
Na_2O	0.10	0.10	0.10	0.10	0.11	0.12	0.11	0.12	0.11	0.08	0.11	0.10	0.11
TiO_2	0.10	0.10	0.10	0.10	0.09	0.11	0.08	0.37	0.10	0.23	0.17	0.17	0.17
MnO	0.12	0.13	0.12	0.12	0.12	0.12	0.12	0.12	0.12	0.13	0.14	0.14	0.14
Cr_2O_3	0.55	0.55	0.55	0.55	0.71	0.67	0.71	0.61	0.72	0.65	0.44	0.44	0.44
Total	100.27	100.18	100.47	99.67	100.23	100.32	99.92	99.72	99.95	99.59	100.56	100.25	99.76
Mg ratio= Mg/(Mg+SFe)	.90	.90	.90	.90	.91	.91	.91	.91	.91	.90	.89	.89	.89
Pyroxene structural formula													
Si	1.87	1.87	1.88	1.87	1.89	1.89	1.89	1.87	1.90	1.90	1.86	1.88	1.87
Al^{IV}	0.13	0.13	0.12	0.13	0.11	0.11	0.11	0.13	0.10	0.10	0.14	0.12	0.13
Al^{VI}	0.073	0.072	0.077	0.068	0.037	0.034	0.039	0.049	0.044	0.032	0.074	0.087	0.087
Fe^{II}	0.175	0.180	0.178	0.178	0.161	0.161	0.159	0.163	0.164	0.176	0.197	0.201	0.200
Mg	1.673	1.670	1.666	1.673	1.716	1.719	1.716	1.701	1.707	1.711	1.652	1.639	1.637
Mn	0.004	0.004	0.003	0.004	0.003	0.003	0.004	0.004	0.004	0.004	0.004	0.004	0.004
Ti	0.003	0.003	0.003	0.003	0.002	0.003	0.002	0.010	0.003	0.006	0.004	0.004	0.006
Cr	0.015	0.015	0.015	0.015	0.019	0.018	0.019	0.017	0.020	0.018	0.012	0.012	0.012
Ca	0.048	0.048	0.048	0.048	0.048	0.048	0.048	0.044	0.048	0.045	0.044	0.044	0.045
Na	0.007	0.007	0.007	0.007	0.007	0.008	0.007	0.008	0.007	0.005	0.007	0.007	0.007
En	89.08	87.91	87.91	87.88	88.89	88.92	88.99	88.91	90.71	90.43	89.39	88.05	88.06
Fs	9.40	9.56	9.56	9.59	8.64	8.61	8.52	6.39	6.74	7.22	8.21	9.56	9.54
Wo	2.52	2.52	2.52	2.53	2.48	2.47	2.49	2.39	2.55	2.36	2.40	2.39	2.40
CaTs [2]	13.43	13.15	12.96	13.63	11.43	11.69	11.25	12.59	10.70	9.93	14.01	12.77	12.94
Papike A/R [3]	A	A	A	A	A	A	A	A	A	A	A	A	A

[1] Total Fe expressed as FeO.
[2] Content of calcium-Tschermak's molecule.
[3] Analysis accepted (A) or rejected (R) by Cameron and Papike (1981) criteria. All "R" analyses listed were rejected on the basis of one criterion and are indistinguishable from "A" analyses.

Table 6. Compositions of amphibole (kaersutite).

Sample No.	Amphibole megacrysts from location 13 (exposures X, Y, Z-AM)[1]														
	X1-AM1	X1-AM2	X1-AM3	X2-AM1	X2-AM2	X3-AM1	X3-AM2	X3-AM3	X4-AM1	X4-AM2	X4-AM3	X4-AM4	X4-AM5	X4-AM6	X4-AM7
Analyses (weight percent oxide)															
SiO_2	37.7	38.4	37.8	38.8	38.1	40.7	40.6	38.5	38.5	37.8	37.9	37.5	38.0	37.7	38.4
Al_2O_3	15.7	14.5	14.8	14.6	14.7	14.7	14.5	14.6	14.9	15.0	15.1	15.0	15.0	15.0	14.9
FeO^{tot} [2]	11.7	9.8	9.4	8.5	9.5	7.9	8.7	8.8	9.0	8.9	9.0	8.9	9.0	8.9	9.0
MgO	12.2	13.1	13.9	13.9	14.1	13.8	13.4	13.7	14.1	13.9	13.8	13.8	13.8	13.7	13.6
CaO	12.2	11.5	12.2	11.5	12.2	10.9	11.0	11.6	12.0	11.9	11.7	12.1	12.0	12.0	12.0
Na_2O	2.7	2.6	2.6	2.5	2.5	2.3	2.3	2.5	2.6	2.6	2.6	2.6	2.6	2.6	2.6
K_2O	1.3	1.9	2.0	2.0	2.0	2.0	2.0	2.0	2.0	2.0	2.0	2.0	2.0	2.0	2.0
TiO_2	3.9	5.5	5.9	5.6	5.9	5.7	5.6	5.6	5.8	5.9	5.9	5.9	5.9	5.9	5.8
Cr_2O_3	0.04	0.02	0.03	0.04	0.04	0.23	0.03	0.02	0.11	0.12	0.12	0.11	0.11	0.12	0.11
Total	97.44	97.32	98.63	97.44	99.04	98.23	98.13	97.32	99.01	98.12	98.12	97.91	98.41	97.92	98.41
Mg ratio= Mg/(Mg+SFe)	.65	.70	.72	.74	.73	.76	.73	.74	.74	.74	.73	.73	.73	.73	.73
Amphibole structural formula—23 oxygens															
Si	5.64	5.72	5.57	5.73	5.59	5.90	5.92	5.71	5.63	5.58	5.59	5.55	5.59	5.58	5.64
Al^{IV}	2.36	2.28	2.43	2.27	2.41	2.10	2.08	2.29	2.37	2.42	2.41	2.45	2.41	2.42	2.36
Al^{VI}	0.41	0.26	0.14	0.27	0.13	0.42	0.41	0.26	0.19	0.19	0.22	0.17	0.20	0.19	0.23
Al^{tot} [3]	2.77	2.54	2.57	2.54	2.54	2.52	2.49	2.55	2.56	2.61	2.63	2.62	2.61	2.61	2.59
Fe^{II}	1.47	1.22	1.16	1.04	1.16	0.96	1.06	1.09	1.10	1.10	1.11	1.10	1.11	1.10	1.11
Mg	2.72	2.91	3.05	3.05	3.08	2.98	2.91	3.03	3.07	3.06	3.03	3.05	3.03	3.02	2.98
Ti	0.44	0.62	0.65	0.62	0.65	0.62	0.61	0.62	0.64	0.66	0.65	0.66	0.65	0.66	0.64
Cr	0.005	0.002	0.004	0.005	0.005	0.03	0.003	0.002	0.013	0.014	0.014	0.013	0.013	0.014	0.013
Ca	1.96	1.83	1.93	1.82	1.92	1.69	1.72	1.84	1.88	1.88	1.85	1.92	1.89	1.90	1.89
Na	0.78	0.74	0.74	0.71	0.71	0.64	0.65	0.72	0.74	0.74	0.74	0.75	0.74	0.75	0.74
K	0.25	0.36	0.38	0.38	0.37	0.37	0.37	0.38	0.37	0.38	0.38	0.38	0.38	0.38	0.38
Papike A/R[4]	R	A	R	A	R	A	A	A	A	A	A	R	A	R	R

Table 6. Compositions of amphibole (kaersutite)—Continued.

Sample No.	Amphibole megacrysts from location 13 (exposures X, Y, Z-AM)[1]—continued												
	X4-AM8	X4-AM9	X4-AM10	X5-AM1	Y1-AM1	Y2-AM1	Y3-AM1	Y3-AM2	Y3-AM3	Y3-AM4	Y3-AM5	Y3-AM6	Y5-AM1
Analyses (weight percent oxide)													
SiO_2	37.4	37.4	38.1	38.6	40.1	40.2	39.9	40.2	40.0	40.6	40.1	40.8	40.2
Al_2O_3	15.0	14.9	14.5	14.8	14.7	14.7	14.7	14.7	14.7	14.6	14.4	14.6	14.8
FeO^{tot} [2]	9.0	10.0	10.4	8.4	8.4	8.2	8.8	8.8	9.3	8.3	10.9	8.1	8.3
MgO	13.6	13.0	12.6	13.8	13.9	13.9	13.7	13.7	13.4	13.9	12.1	13.9	14.0
CaO	12.0	12.0	11.5	11.5	11.0	11.0	11.0	11.0	11.0	11.0	11.0	11.0	11.0
Na_2O	2.6	2.6	2.6	2.5	2.4	2.3	2.4	2.4	2.4	2.3	2.4	2.3	2.4
K_2O	2.0	2.0	1.9	2.0	2.0	2.0	2.0	2.0	2.0	2.0	1.9	2.0	2.0
TiO_2	6.0	5.9	5.5	5.6	5.6	5.8	5.7	5.6	5.6	5.7	5.6	5.8	5.7
Cr_2O_3	0.12	0.02	0.02	0.11	0.05	0.16	0.03	0.03	0.02	0.06	0.03	0.13	0.05
Total	97.72	97.82	97.12	97.31	98.15	98.26	98.23	98.43	98.42	98.46	98.43	98.63	98.45
Mg ratio= Mg/(Mg+SFe)	.74	.74	.68	.75	.75	.75	.73	.74	.72	.75	.66	.75	.75
Amphibole structural formula—23 oxygens													
Si	5.55	5.57	5.70	5.71	5.84	5.84	5.82	5.85	5.84	5.89	5.89	5.90	5.84
Al^{IV}	2.45	2.43	2.30	2.29	2.16	2.16	2.18	2.15	2.16	2.11	2.11	2.10	2.16
Al^{VI}	0.18	0.19	0.26	0.29	0.37	0.36	0.35	0.37	0.37	0.38	0.38	0.39	0.37
Al^{tot} [3]	2.63	2.62	2.56	2.58	2.53	2.52	2.53	2.52	2.53	2.49	2.50	2.49	2.53
Fe^{II}	1.12	1.25	1.30	1.04	1.02	1.00	1.07	1.07	1.14	1.01	1.34	0.98	1.01
Mg	3.01	2.88	2.81	3.04	3.02	3.01	2.98	2.97	2.92	3.00	2.65	3.00	3.03
Ti	0.67	0.66	0.62	0.62	0.61	0.63	0.63	0.61	0.62	0.62	0.62	0.63	0.62
Cr	0.014	0.002	0.002	0.013	0.006	0.02	0.002	0.002	0.004	0.007	0.002	0.015	0.006
Ca	1.91	1.91	1.834	1.82	1.72	1.71	1.72	1.71	1.72	1.71	1.73	1.70	1.71
Na	0.75	0.74	0.75	0.71	0.68	0.68	0.64	0.68	0.67	0.65	0.68	0.65	0.67
K	0.38	0.38	0.36	0.38	0.37	0.37	0.36	0.37	0.37	0.37	0.36	0.37	0.37
Papike A/R[4]	R	R	A	A	A	A	A	A	A	A	A	A	A

Table 6. Compositions of amphibole (kaersutite)—Continued.

Sample No.	Amphibole megacrysts from location 13 (exposures X, Y, Z-AM)[1]—continued														
	Z1-AM1	Z2-AM1	Z3-AM1	Z3-AM2	Z4-AM1	Z4-AM2	Z4-AM3	Z4-AM4	Z4-AM5	Z4-AM6	Z4-AM7	Z4-AM8	Z4-AM9	Z4-AM10	Z4-AM11
Analyses (weight percent oxide)															
SiO_2	40.0	40.0	39.5	39.6	40.0	39.8	40.6	40.9	41.0	40.8	40.6	41.1	40.5	41.0	40.1
Al_2O_3	14.4	14.4	14.4	14.4	14.5	14.4	14.5	14.7	14.8	14.7	14.6	14.6	14.6	14.6	14.4
$FeO^{tot\,2}$	7.9	8.1	9.8	9.2	8.2	8.5	9.0	8.8	8.3	8.7	8.2	8.6	9.9	8.3	11.0
MgO	13.7	13.7	12.6	13.0	13.7	13.4	13.2	13.6	13.9	13.6	13.7	13.8	12.9	13.9	12.1
CaO	10.8	10.8	10.9	10.8	10.8	10.9	11.0	11.0	11.0	11.0	11.0	11.0	11.1	11.0	10.9
Na_2O	2.3	2.3	2.4	2.4	2.4	2.4	2.3	2.4	2.3	2.3	2.3	2.3	2.4	2.3	2.4
K_2O	2.0	2.0	2.0	2.0	2.0	2.0	2.0	2.0	2.0	2.0	2.0	2.0	1.9	2.0	2.0
TiO_2	5.6	5.6	5.5	5.6	5.8	5.7	5.6	5.7	5.7	5.6	5.6	5.7	5.6	5.8	5.5
Cr_2O_3	0.20	0.14	0.03	0.04	0.08	0.04	0.03	0.03	0.04	0.03	0.05	0.04	0.03	0.08	0.03
Total	96.90	97.04	97.13	97.04	97.48	97.14	98.23	99.13	99.04	98.73	98.05	99.14	98.93	98.98	98.43
Mg ratio= Mg/(Mg+SFe)	.76	.75	.70	.72	.75	.74	.72	.73	.75	.74	.75	.74	.70	.75	.66
Amphibole structural formula—23 oxygens															
Si	5.89	5.88	5.86	5.86	5.86	5.87	5.92	5.90	5.90	5.91	5.91	5.92	5.89	5.91	5.89
Al^{IV}	2.11	2.12	2.14	2.14	2.14	2.13	2.08	2.10	2.10	2.09	2.09	2.08	2.11	2.09	2.11
Al^{VI}	0.39	0.38	0.38	0.38	0.37	0.37	0.41	0.40	0.42	0.42	0.41	0.40	0.39	0.39	0.39
Al^{tot3}	2.50	2.50	2.52	2.52	2.51	2.50	2.49	2.50	2.52	2.51	2.50	2.48	2.50	2.48	2.50
Fe^{II}	0.97	1.00	1.22	1.14	1.00	1.05	1.10	1.06	1.00	1.05	1.00	1.04	1.20	1.00	1.35
Mg	3.01	3.00	2.79	2.87	2.99	2.94	2.87	2.92	2.98	2.93	2.97	2.96	2.80	2.99	2.65
Ti	0.62	0.62	0.61	0.62	0.64	0.63	0.61	0.62	0.62	0.61	0.61	0.62	0.61	0.63	0.61
Cr	0.023	0.016	0.004	0.005	0.009	0.005	0.004	0.003	0.005	0.003	0.006	0.005	0.003	0.009	0.004
Ca	1.70	1.70	1.73	1.71	1.70	1.72	1.72	1.70	1.70	1.71	1.72	1.70	1.73	1.70	1.72
Na	0.66	0.66	0.68	0.69	0.68	0.69	0.65	0.67	0.64	0.65	0.64	0.64	0.68	0.65	0.68
K	0.37	0.38	0.38	0.38	0.37	0.38	0.37	0.37	0.36	0.37	0.37	0.37	0.35	0.37	0.38
Papike A/R[4]	A	A	A	A	A	A	A	A	A	A	A	A	A	A	A

Table 6. Compositions of amphibole (kaersutite)—Continued.

Sample No.	Amphibole megacrysts from location 13 (exposures X, Y, Z-AM)[1]—continued					Euhedral grains (EG) and megacrysts (AM) from other dikes									
	Z5-AM1	Z5-AM2	Z5-AM3	Z5-AM4	Z5-AM5	EG2	EG3	EG7	AM1	AM2	AM4	AM5	AM6	AM7	AM8
Analyses (weight percent oxide)															
SiO_2	39.6	40.7	41.1	40.5	40.0	41.5	41.8	40.2	40.5	40.6	41.2	39.2	39.1	40.4	41.0
Al_2O_3	14.4	14.6	14.8	14.5	14.5	14.4	14.3	14.5	14.5	14.5	14.3	14.7	15.1	14.9	14.9
FeO^{tot}[2]	8.9	9.5	8.3	10.0	8.8	8.6	8.9	9.2	8.3	8.9	9.7	10.7	10.7	10.0	8.5
MgO	13.3	13.2	13.9	12.9	13.2	13.5	13.4	13.3	13.8	13.5	12.9	12.7	12.5	13.0	13.9
CaO	10.9	11.1	11.1	11.0	10.9	11.1	11.2	11.0	11.0	11.1	11.1	11.7	11.6	11.2	11.3
Na_2O	2.4	2.4	2.3	2.4	2.4	2.3	2.3	2.3	2.3	2.4	2.4	2.5	2.6	2.5	2.4
K_2O	2.0	2.0	2.0	1.9	2.0	2.0	2.0	2.0	2.0	2.0	2.0	1.4	1.4	2.0	2.0
TiO_2	5.6	5.6	5.7	5.6	5.7	5.8	5.7	5.6	5.8	5.7	5.7	4.0	4.1	5.6	5.6
Cr_2O_3	0.04	0.02	0.09	0.03	0.04	0.04	0.03	0.03	0.09	0.03	0.03	0.01	0.00	0.00	0.01
Total	97.14	99.12	99.29	98.83	97.54	99.24	99.63	98.13	98.39	98.73	99.53	96.91	97.10	99.60	99.61
Mg ratio= Mg/(Mg+SFe)	.73	.71	.75	.70	.73	.74	.73	.72	.75	.73	.70	.68	.67	.70	.74
Amphibole structural formula—23 oxygens															
Si	5.85	5.90	5.90	5.90	5.88	5.97	5.99	5.88	5.88	5.89	5.94	5.85	5.81	5.85	5.88
Al^{IV}	2.15	2.10	2.10	2.10	2.12	2.03	2.01	2.12	2.12	2.11	2.06	2.15	2.19	2.15	2.12
Al^{VI}	0.36	0.39	0.41	0.38	0.39	0.41	0.41	0.38	0.38	0.37	0.41	0.44	0.47	0.38	0.40
Al^{tot}[3]	2.51	2.49	2.51	2.48	2.51	2.44	2.42	2.50	2.50	2.48	2.47	2.59	2.66	2.53	2.52
Fe^{II}	1.10	1.15	1.00	1.22	1.08	1.03	1.07	1.12	1.01	1.08	1.17	1.33	1.34	1.20	1.02
Mg	2.93	2.85	2.98	2.80	2.89	2.89	2.86	2.90	2.98	2.92	2.77	2.82	2.77	2.80	2.97
Ti	0.62	0.61	0.62	0.61	0.63	0.63	0.62	0.62	0.63	0.62	0.62	0.45	0.45	0.61	0.60
Cr	0.005	0.002	0.010	0.004	0.005	0.004	0.003	0.004	0.010	0.003	0.003	0.000	0.000	0.000	0.000
Ca	1.72	1.72	1.71	1.72	1.72	1.71	1.72	1.72	1.71	1.73	1.72	1.87	1.86	1.74	1.74
Na	0.69	0.68	0.64	0.68	0.60	0.64	0.64	0.65	0.65	0.67	0.67	0.72	0.75	0.70	0.66
K	0.38	0.37	0.37	0.35	0.38	0.37	0.37	0.37	0.37	0.37	0.37	0.27	0.27	0.37	0.37
Papike A/R[4]	A	A	A	A	A	R	R	A	A	A	R	A	A	A	A

Table 6. Compositions of amphibole (kaersutite)—Continued.

Sample No.	Amphibole vein in lherzolite xenolith (BC-2-21)							Amphibole of kaersutite-phlogopite-apatite cluster (KPA)	
	A1	A2	A3	A4	A5	A6	A7	KPA-A1	KPA-A2
Analyses (weight percent oxide)									
SiO_2	40.2	40.1	40.0	40.1	39.9	40.1	39.9	39.5	39.5
Al_2O_3	14.7	14.7	14.7	14.7	14.7	14.7	14.5	14.4	14.4
FeO^{tot}[2]	9.3	9.3	9.3	9.3	9.3	9.3	10.2	14.2	14.2
MgO	13.4	13.4	13.3	13.4	13.3	13.4	12.8	9.9	9.9
CaO	11.0	11.0	11.0	11.0	11.0	11.0	11.0	10.8	10.8
Na_2O	2.4	2.4	2.4	2.4	2.4	2.4	2.4	2.6	2.5
K_2O	2.0	2.0	2.0	2.0	2.0	2.0	1.9	1.8	1.8
TiO_2	5.6	5.6	5.6	5.6	5.5	5.6	5.6	5.2	5.2
Cr_2O_3	0.03	0.03	0.04	0.02	0.03	0.03	0.03	0.03	0.03
Total	98.63	98.53	98.34	98.52	98.13	98.53	98.33	98.43	98.33
Mg ratio= Mg/(Mg+SFe)	.72	.72	.72	.72	.72	.72	.69	.56	.56
Amphibole structural formula—23 oxygens									
Si	5.85	5.84	5.84	5.85	5.84	5.84	5.85	5.89	5.90
Al^{IV}	2.15	2.16	2.16	2.15	2.16	2.16	2.15	2.11	2.10
Al^{VI}	0.38	0.37	0.37	0.37	0.38	0.37	0.36	0.42	0.43
Al^{tot}[3]	2.53	2.53	2.53	2.52	2.54	2.53	2.51	2.53	2.53
Fe^{II}	1.13	1.13	1.14	1.13	1.14	1.13	1.25	1.77	1.77
Mg	2.91	2.91	2.89	2.91	2.90	2.91	2.80	2.20	2.20
Ti	0.61	0.61	0.62	0.61	0.61	0.61	0.62	0.58	0.58
Cr	0.003	0.004	0.005	0.002	0.004	0.004	0.004	0.004	0.004
Ca	1.72	1.72	1.72	1.72	1.73	1.72	1.73	1.73	1.73
Na	0.67	0.68	0.68	0.68	0.68	0.68	0.68	0.75	0.72
K	0.37	0.37	0.37	0.37	0.37	0.37	0.36	0.34	0.34
Papike A/R[4]	A	A	A	A	A	A	A	R	A

[1]Numbering of amphibole megacrysts (AM) from dike: prefix X, Y, Z refers to exposures, and numbers 1-5 are zones.
[2]Total Fe expressed as FeO.
[3]Total Al is a plotting parameter in figure 16A.
[4]Analysis accepted (A) or rejected (R) by Papike and others (1969) screen for amphibole probe analyses. All "R" analyses listed were rejected on the basis of one criterion and are indistinguishable from "A" analyses.

* U.S. GOVERNMENT PRINTING OFFICE: 1994-583-048/80015

SELECTED SERIES OF U.S. GEOLOGICAL SURVEY PUBLICATIONS

Periodicals

Earthquakes & Volcanoes (issued bimonthly).
Preliminary Determination of Epicenters (issued monthly).

Technical Books and Reports

Professional Papers are mainly comprehensive scientific reports of wide and lasting interest and importance to professional scientists and engineers. Included are reports on the results of resource studies and of topographic, hydrologic, and geologic investigations. They also include collections of related papers addressing different aspects of a single scientific topic.

Bulletins contain significant data and interpretations that are of lasting scientific interest but are generally more limited in scope or geographic coverage than Professional Papers. They include the results of resource studies and of geologic and topographic investigations, as well as collections of short papers related to a specific topic.

Water-Supply Papers are comprehensive reports that present significant interpretive results of hydrologic investigations of wide interest to professional geologists, hydrologists, and engineers. The series covers investigations in all phases of hydrology, including hydrogeology, availability of water, quality of water, and use of water.

Circulars present administrative information or important scientific information of wide popular interest in a format designed for distribution at no cost to the public. Information is usually of short-term interest.

Water-Resource Investigations Reports are papers of an interpretive nature made available to the public outside the formal USGS publications series. Copies are reproduced on request unlike formal USGS publications, and they are also available for public inspection at depositories indicated in USGS catalogs.

Open-File Reports include unpublished manuscript reports, maps, and other material that are made available for public consultation at depositories. They are a nonpermanent form of publication that may be cited in other publications as sources of information.

Maps

Geologic Quadrangle Maps are multicolor geologic maps on topographic bases in 7 1/2- or 15-minute quadrangle formats (scales mainly 1:24,000 or 1:62,500) showing bedrock, surficial, or engineering geology. Maps generally include brief texts; some maps include structure and columnar sections only.

Geophysical Investigations Maps are on topographic or planimetric bases at various scales; they show results of surveys using geophysical techniques, such as gravity, magnetic, seismic, or radioactivity, which reflect subsurface structures that are of economic or geologic significance. Many maps include correlations with the geology.

Miscellaneous Investigations Series Maps are on planimetric or topographic bases of regular and irregular areas at various scales; they present a wide variety of format and subject matter. The series also includes 7 1/2-minute quadrangle photogeologic maps on planimetric bases that show geology as interpreted from aerial photographs. Series also includes maps of Mars and the Moon.

Coal Investigations Maps are geologic maps on topographic or planimetric bases at various scales showing bedrock or surficial geology, stratigraphy, and structural relations in certain coal-resource areas.

Oil and Gas Investigations Charts show stratigraphic information for certain oil and gas fields and other areas having petroleum potential.

Miscellaneous Field Studies Maps are multicolor or black-and-white maps on topographic or planimetric bases on quadrangle or irregular areas at various scales. Pre-1971 maps show bedrock geology in relation to specific mining or mineral-deposit problems; post-1971 maps are primarily black-and-white maps on various subjects, such as environmental studies or wilderness mineral investigations.

Hydrologic Investigations Atlases are multicolor or black-and-white maps on topographic or planimetric bases presenting a wide range of geohydrologic data of both regular and irregular areas; principal scale is 1:24,000, and regional studies are at 1:250,000 scale or smaller.

Catalogs

Permanent catalogs, as well as some others, giving comprehensive listings of U.S. Geological Survey publications are available under the conditions indicated below from the U.S. Geological Survey, Books and Open-File Reports Sales, Federal Center, Box 25286, Denver, CO 80225. (See latest Price and Availability List.)

"Publications of the Geological Survey, 1879-1961" may be purchased by mail and over the counter in paperback book form and as a set of microfiche.

"Publications of the Geological Survey, 1962-1970" may be purchased by mail and over the counter in paperback book form and as a set of microfiche.

"Publications of the Geological Survey, 1971-1981" may be purchased by mail and over the counter in paperback book form (two volumes, publications listing and index) and as a set of microfiche.

Supplements for 1982, 1983, 1984, 1985, 1986, and for subsequent years since the last permanent catalog may be purchased by mail and over the counter in paperback book form.

State catalogs, "List of U.S. Geological Survey Geologic and Water-Supply Reports and Maps For (State)," may be purchased by mail and over the counter in paperback booklet form only.

"Price and Availability List of U.S. Geological Survey Publications," issued annually, is available free of charge in paperback booklet form only.

Selected copies of a monthly catalog "New Publications of the U.S. Geological Survey" are available free of charge by mail or may be obtained over the counter in paperback booklet form only. Those wishing a free subscription to the monthly catalog "New Publications of the U.S. Geological Survey" should write to the U.S. Geological Survey, 582 National Center, Reston, VA 22092.

Note.--Prices of Government publications listed in older catalogs, announcements, and publications may be incorrect. Therefore, the prices charged may differ from the prices in catalogs, announcements, and publications.


U.S. DEPARTMENT OF THE INTERIOR
MARCH 3, 1849